

Thermochemical Non-Equilibrium Entry Flows in Mars in Three-Dimensions – Part I

Edisson S. G. Maciel, Amilcar P. Pimenta, and Nikos E. Mastorakis

Abstract—This work describes a numerical tool to perform thermochemical non-equilibrium simulations of reactive flow in three-dimensions. The Van Leer and Liou and Steffen Jr. schemes, in their first- and second-order versions, are implemented to accomplish the numerical simulations. The Euler and Navier-Stokes equations, on a finite volume context and employing structured and unstructured spatial discretizations, are applied to solve the “hot gas” hypersonic flow around a blunt body, in three-dimensions. The second-order version of the Van Leer and Liou and Steffen Jr. schemes are obtained from a “MUSCL” extrapolation procedure in a context of structured spatial discretization. In the unstructured context, only first-order solutions are obtained. The convergence process is accelerated to the steady state condition through a spatially variable time step procedure, which has proved effective gains in terms of computational acceleration. The reactive simulations involve a Mars atmosphere chemical model of nine species: N, O, N₂, O₂, NO, CO₂, C, CO, and CN, based on the work of Kay and Netterfield. Fifty-three chemical reactions, involving dissociation and recombination, are simulated by the proposed model. The Arrhenius formula is employed to determine the reaction rates and the law of mass action is used to determine the source terms of each gas species equation. The results have indicated the Van Leer TVD scheme as presenting good solutions, both inviscid and viscous cases.

Keywords— Thermochemical non-equilibrium, Mars entry, Nine species model, Hypersonic “hot gas” flow, Finite volume, Euler and Navier-Stokes equations, Three-dimensions.

I. INTRODUCTION

THERE has been significant interest in recent years in a mission to Mars. One such proposal is the MARSNET assessment study [1] concerning the potential contribution of ESA (European Space Agency) to a Mars Network mission in cooperation with NASA. NASA is currently studying a network mission MESUR (Mars Environmental Survey), involving the placement of up twenty small scientific stations

Edisson S. G. Maciel works as a post-doctorate researcher at ITA (Aeronautical Technological Institute), Aeronautical Engineering Division – Praça Marechal do Ar Eduardo Gomes, 50 – Vila das Acácias – São José dos Campos – SP – Brazil – 12228-900 (corresponding author, phone number: +55 012 99165-3565; e-mail: edisavio@edissonsavio.eng.br).

Amilcar P. Pimenta teaches at ITA (Aeronautical Technological Institute), Aeronautical Engineering Division – Praça Marechal do Ar Eduardo Gomes, 50 – Vila das Acácias – São José dos Campos – SP – Brazil – 12228-900 (e-mail: amilcar@ita.br).

Nikos E. Mastorakis is with WSEAS (World Scientific and Engineering Academy and Society), A. I. Theologou 17-23, 15773 Zografou, Athens, Greece, E-mail: mastor@wseas.org as well as with the Technical University of Sofia, Industrial Engineering Department, Sofia, 1000, Bulgaria mailto:mastor@tu-sofia.bg

on the surface of Mars. The objective of the proposed ESA activities is the provision of three of these stations to perform a variety of scientific experiments. The intended entry scenario is an unguided ballistic entry at a typical velocity of 6 km/s using a blunt sphere/cone configuration in which deceleration is provided predominantly by hypersonic aero-braking. It is important that the mass of the vehicle structure and thermal protection system (TPS) be minimized such that the payload delivered to the surface may be maximized.

The trajectory for a ballistic Martian entry takes the vehicle through regions where thermochemical non-equilibrium effects in the surrounding shock layer may be significant. For typical entry velocities (> 5 km/s) the temperature in the shock layer will be sufficiently high for dissociation of the freestream species to occur. The energy removed through such reactions may be released at the vehicle surface via recombination leading to significantly enhanced heat transfer rates. In order to design the TPS for minimum mass the heat transfer rate needs to be accurately predicted. This requires that any catalytic properties of the TPS material are accounted for in the heat transfer rate calculation since these will determine the extent of wall recombination.

As aforementioned, missions to other planets remain an objective for the ESA, and such missions generally involve the entry of a space vehicle into the atmospheres of those planets. In the context of such entry, aerothermodynamics is one of the critical technologies. While the thermochemical behavior of air under re-entry conditions has been studied extensively, and is to some degree understood, the same is not true for entries into other atmospheres. The atmospheres of Mars and Venus, for example, contain significant amounts of carbon dioxide. In particular, the Mars atmosphere is a mixture of approximately 96% CO₂ and 4% N₂, with pressures much lower than the Earth’s atmosphere, so for any entry into the Martian atmosphere the non-equilibrium behavior of CO₂ is likely to be of importance for a typical blunt body entry vehicle. This includes not just the influence of thermochemistry on the forebody heatshield flowfield, but also the influence on the shoulder expansion, base flow, and base heating environment.

Analyzing the reentry flows in Earth, [2] have proposed a numerical tool implemented to simulate inviscid and viscous flows employing the reactive gas formulation of thermal and chemical non-equilibrium in two-dimensions. The [3] numerical algorithm was implemented to perform the numerical experiments. The Euler and Navier-Stokes equations, employing a finite volume formulation, on the context of structured and unstructured spatial discretizations,

were solved. These variants allowed an effective comparison between the two types of spatial discretization aiming verify their potentialities: solution quality, convergence speed, computational cost, etc. The aerospace problem involving the hypersonic flow around a blunt body, in two-dimensions, was simulated. The reactive simulations involved an air chemical model of five species: N, O, N₂, O₂ and NO. Seventeen chemical reactions, involving dissociation and recombination, were simulated by the proposed model. The Arrhenius formula was employed to determine the reaction rates and the law of mass action was used to determine the source terms of each gas species equation. A spatially variable time step was employed aiming to obtain gains in terms of convergence acceleration. Such gains were demonstrated in [4-5]. Good results were obtained with such code.

[6] have presented a numerical tool implemented to simulate inviscid and viscous flows employing the reactive gas formulation of thermal and chemical non-equilibrium in three-dimensions. The [3] numerical algorithm was implemented to perform the numerical experiments. The Euler and Navier-Stokes equations, employing a finite volume formulation, on the context of structured and unstructured spatial discretizations, were solved. The aerospace problem involving the hypersonic “hot gas” flow around a blunt body, in three-dimensions, was simulated. The reactive simulations involved an air chemical model of five species: N, O, N₂, O₂ and NO. Seventeen chemical reactions, involving dissociation and recombination, were simulated by the proposed model. The Arrhenius formula was employed to determine the reaction rates and the law of mass action was used to determine the source terms of each gas species equation. A spatially variable time step was employed aiming to obtain gains in terms of convergence acceleration. Such gains were demonstrated in [4-5]. In that first part, only the structured solutions were presented. The unstructured solutions will be shown in the second part of such study.

[7] have proposed a numerical tool implemented to simulate inviscid and viscous flows employing the reactive gas formulation of thermochemical non-equilibrium in three-dimensions. The [3] and [8] numerical algorithms were implemented to perform the numerical experiments. The Euler and Navier-Stokes equations, employing a finite volume formulation, on the context of structured and unstructured spatial discretizations, are solved. The aerospace problem involving the hypersonic flow around a blunt body, in three-dimensions, was simulated. The reactive simulations involved an air chemical model of seven species: N, O, N₂, O₂, NO, NO⁺ and e⁻. Eighteen chemical reactions, involving dissociation, recombination and ionization, were simulated by the proposed model. Such model was suggested by Blotner ([9]). The Arrhenius formula was employed to determine the reaction rates and the law of mass action was used to determine the source terms of each gas species equation. A spatially variable time step was employed aiming to obtain gains in terms of convergence acceleration. Such gains were demonstrated in [4-5]. In this work, it was only presented the structured formulation and solutions. The unstructured

formulation and solutions will be presented in the second part of this study, which treats exclusively the unstructured context.

This work, first part of this study, describes a numerical tool to perform thermochemical non-equilibrium simulations of reactive flows in three-dimensions in Mars atmosphere. The [3; 8] schemes, in their first- and second-order versions, are implemented to accomplish the numerical simulations. The Euler and Navier-Stokes equations, on a finite volume context and employing structured and unstructured spatial discretizations, are applied to solve the “hot gas” hypersonic flow around a blunt body, in three-dimensions. The second-order version of the [3; 8] schemes are obtained from a “MUSCL” extrapolation procedure (details in [10]) in a context of structured spatial discretization. In the unstructured context, only first-order solutions are obtained. The convergence process is accelerated to the steady state condition through a spatially variable time step procedure, which has proved effective gains in terms of computational acceleration (see [4-5]).

The reactive simulations involve a Mars atmosphere chemical model of nine species: N, O, N₂, O₂, NO, CO₂, C, CO, and CN. Fifty-three chemical reactions, involving dissociation and recombination, are simulated by the proposed model. The Arrhenius formula is employed to determine the reaction rates and the law of mass action is used to determine the source terms of each gas species equation.

The results have demonstrated that the most conservative scheme is due to [8], although the [3] scheme is more robust, providing results to the second-order viscous case. Moreover, the [3] scheme presents the best mass fraction profiles at the stagnation line, characterizing discrete dissociation of CO₂ and formation of CO.

II. FORMULATION TO REACTIVE FLOW IN THERMOCHEMICAL NON-EQUILIBRIUM

A. Reactive Equations in Three-Dimensions

The reactive Navier-Stokes equations in thermal and chemical non-equilibrium were implemented on a finite volume context, in the three-dimensional space. In this case, these equations in integral and conservative forms can be expressed by:

$$\frac{\partial}{\partial t} \int_V Q dV + \int_S \vec{F} \cdot \vec{n} dS = \int_V S_{CV} dV, \text{ with}$$

$$\vec{F} = (E_e - E_v) \vec{i} + (F_e - F_v) \vec{j} + (G_e - G_v) \vec{k}, \quad (1)$$

where: Q is the vector of conserved variables, V is the volume of a computational cell, \vec{F} is the complete flux vector, \vec{n} is the unity vector normal to the flux face, S is the flux area, S_{CV} is the chemical and vibrational source term, E_e, F_e and G_e are the convective flux vectors or the Euler flux vectors in the x, y and z directions, respectively, E_v, F_v and G_v are the viscous flux vectors in the x, y and z directions, respectively. The \vec{i} , \vec{j}

and \bar{k} unit vectors define the Cartesian coordinate system. Fourteen (14) conservation equations are solved: one of general mass conservation, three of linear momentum conservation, one of total energy, eight of species mass conservation and one of the vibrational internal energy of the molecules. Therefore, one of the species is absent of the iterative process. The CFD (“Computational Fluid Dynamics”) literature recommends that the species of biggest mass fraction of the gaseous mixture should be omitted, aiming to result in a minor numerical accumulation error, corresponding to the biggest mixture constituent (in this case, the Mars atmosphere). To the present study, in which is chosen a chemical model to the Mars atmosphere composed of nine (9) chemical species (N, O, N₂, O₂, NO, CO₂, C, CO, and CN) and fifty-three (53) chemical reactions, this species is the CO₂. The vectors Q, E_e, F_e, G_e, E_v, F_v, G_v and S_{CV} can, hence, be defined as follows ([11]):

$$Q = \begin{Bmatrix} \rho \\ \rho u \\ \rho v \\ \rho w \\ e \\ \rho_1 \\ \rho_2 \\ \rho_3 \\ \rho_4 \\ \rho_5 \\ \rho_7 \\ \rho_8 \\ \rho_9 \\ \rho e_v \end{Bmatrix}, \quad E_e = \begin{Bmatrix} \rho u \\ \rho u^2 + p \\ \rho uv \\ \rho uw \\ \rho Hu \\ \rho_1 u \\ \rho_2 u \\ \rho_3 u \\ \rho_4 u \\ \rho_5 u \\ \rho_7 u \\ \rho_8 u \\ \rho_9 u \\ \rho e_v u \end{Bmatrix}; \quad (2)$$

$$F_e = \begin{Bmatrix} \rho v \\ \rho vu \\ \rho v^2 + p \\ \rho vw \\ \rho Hv \\ \rho_1 v \\ \rho_2 v \\ \rho_3 v \\ \rho_4 v \\ \rho_5 v \\ \rho_7 v \\ \rho_8 v \\ \rho_9 v \\ \rho e_v v \end{Bmatrix}; \quad G_e = \begin{Bmatrix} \rho w \\ \rho wu \\ \rho wv \\ \rho w^2 + p \\ \rho Hw \\ \rho_1 w \\ \rho_2 w \\ \rho_3 w \\ \rho_4 w \\ \rho_5 w \\ \rho_7 w \\ \rho_8 w \\ \rho_9 w \\ \rho e_v w \end{Bmatrix}; \quad (3)$$

in which: ρ is the mixture density; u , v and w are Cartesian components of the velocity vector in the x , y and z directions,

respectively; p is the fluid static pressure; e is the fluid total energy; $\rho_1, \rho_2, \rho_3, \rho_4, \rho_5, \rho_7, \rho_8$, and ρ_9 are densities of the N, O, N₂, O₂, NO, C, CO and CN, respectively; H is the mixture total enthalpy; e_v is the sum of the vibrational energy of the molecules; the τ 's are the components of the viscous stress tensor; $q_{f,x}, q_{f,y}$ and $q_{f,z}$ are the frozen components of the Fourier-heat-flux vector in the x , y and z directions, respectively; $q_{v,x}, q_{v,y}$ and $q_{v,z}$ are the components of the Fourier-heat-flux vector calculated with the vibrational thermal conductivity and vibrational temperature; $\rho_s v_{sx}, \rho_s v_{sy}$ and $\rho_s v_{sz}$ represent the species diffusion flux, defined by the Fick law; ϕ_x, ϕ_y and ϕ_z are the terms of mixture diffusion; $\phi_{v,x}, \phi_{v,y}$ and $\phi_{v,z}$ are the terms of molecular diffusion calculated at the vibrational temperature; $\dot{\omega}_s$ is the chemical source term of each species equation, defined by the law of mass action; e_v^* is the molecular-vibrational-internal energy calculated with the translational/rotational temperature; and τ_s is the translational-vibrational characteristic relaxation time of each molecule.

$$G_v = \frac{1}{Re} \begin{Bmatrix} 0 \\ \tau_{xz} \\ \tau_{yz} \\ \tau_{zz} \\ \tau_{xz}u + \tau_{yz}v + \tau_{zz}w - q_{f,z} - q_{v,z} - \phi_z \\ -\rho_1 v_{1z} \\ -\rho_2 v_{2z} \\ -\rho_3 v_{3z} \\ -\rho_4 v_{4z} \\ -\rho_5 v_{5z} \\ -\rho_7 v_{7z} \\ -\rho_8 v_{8z} \\ -\rho_9 v_{9z} \\ -q_{v,z} - \phi_{v,z} \end{Bmatrix}, \quad (6)$$

$$S_{CV} = \begin{Bmatrix} 0 \\ 0 \\ 0 \\ 0 \\ 0 \\ \dot{\omega}_1 \\ \dot{\omega}_2 \\ \dot{\omega}_3 \\ \dot{\omega}_4 \\ \dot{\omega}_5 \\ \dot{\omega}_7 \\ \dot{\omega}_8 \\ \dot{\omega}_9 \\ \sum_{s=mol} \rho_s (e_{v,s}^* - e_{v,s}) / \tau_s + \sum_{s=mol} \dot{\omega}_s e_{v,s} \end{Bmatrix}. \quad (7)$$

The viscous stresses, in N/m², are determined, according to a Newtonian fluid model, by:

$$\tau_{xx} = 2\mu \frac{\partial u}{\partial x} - \frac{2}{3}\mu \left(\frac{\partial u}{\partial x} + \frac{\partial v}{\partial y} + \frac{\partial w}{\partial z} \right); \quad (8)$$

$$\tau_{xy} = \mu \left(\frac{\partial u}{\partial y} + \frac{\partial v}{\partial x} \right) \text{ and } \tau_{xz} = \mu \left(\frac{\partial u}{\partial z} + \frac{\partial w}{\partial x} \right); \quad (9)$$

$$\tau_{yy} = 2\mu \frac{\partial v}{\partial y} - \frac{2}{3}\mu \left(\frac{\partial u}{\partial x} + \frac{\partial v}{\partial y} + \frac{\partial w}{\partial z} \right); \quad (10)$$

$$\tau_{yz} = \mu \left(\frac{\partial v}{\partial z} + \frac{\partial w}{\partial y} \right); \quad (11)$$

$$\tau_{zz} = 2\mu \frac{\partial w}{\partial z} - \frac{2}{3}\mu \left(\frac{\partial u}{\partial x} + \frac{\partial v}{\partial y} + \frac{\partial w}{\partial z} \right), \quad (12)$$

in which μ is the fluid molecular viscosity.

The frozen components of the Fourier-heat-flux vector, which considers only thermal conduction, are defined by:

$$q_{f,x} = -k_f \frac{\partial T}{\partial x}, \quad q_{f,y} = -k_f \frac{\partial T}{\partial y}; \quad (13)$$

$$q_{f,z} = -k_f \frac{\partial T}{\partial z}, \quad (14)$$

where k_f is the mixture frozen thermal conductivity, calculated conform presented in section C. The vibrational components of the Fourier-heat-flux vector are calculated as follows:

$$q_{v,x} = -k_v \frac{\partial T_v}{\partial x}, \quad q_{v,y} = -k_v \frac{\partial T_v}{\partial y}; \quad (15)$$

$$q_{v,z} = -k_v \frac{\partial T_v}{\partial z}, \quad (16)$$

in which k_v is the vibrational thermal conductivity and T_v is the vibrational temperature, what characterizes this model as of two temperatures: translational/rotational and vibrational. The calculation of T_v and k_v are presented in section C.

The terms of species diffusion, defined by the Fick law, to a condition of thermal non-equilibrium, are determined by ([11]):

$$\rho_s v_{sx} = -\rho D_s \frac{\partial Y_{MF,s}}{\partial x}, \quad \rho_s v_{sy} = -\rho D_s \frac{\partial Y_{MF,s}}{\partial y}; \quad (17)$$

$$\rho_s v_{sz} = -\rho D_s \frac{\partial Y_{MF,s}}{\partial z}, \quad (18)$$

with “s” referent to a given species, $Y_{MF,s}$ being the molar fraction of the species, defined as:

$$Y_{MF,s} = \frac{\rho_s / M_s}{\sum_{k=1}^{ns} \rho_k / M_k} \quad (19)$$

and D_s is the species-effective-diffusion coefficient.

The diffusion terms ϕ_x , ϕ_y and ϕ_z which appear in the energy equation are defined by ([12]):

$$\phi_x = \sum_{s=1}^{ns} \rho_s v_{sx} h_s, \quad \phi_y = \sum_{s=1}^{ns} \rho_s v_{sy} h_s; \quad (20)$$

$$\phi_z = \sum_{s=1}^{ns} \rho_s v_{sz} h_s, \quad (21)$$

being h_s the specific enthalpy (sensible) of the chemical species “s”. The specific enthalpy is calculated as function of the several modes of internal energy as follows:

$$e_{i,trans} = 3/2 R_s T;$$

$$e_{i,rot} = \begin{cases} 0, & \text{atoms} \\ R_s T, & \text{molecules} \end{cases};$$

$$e_{i,vib} = \begin{cases} 0, & \text{atoms} \\ \frac{R_s \theta_{v,s}}{e^{\theta_{v,s}/T_v} - 1}, & \text{molecules} \end{cases};$$

$$e_{i,0} = \Delta h_{f,s} - R_s T_{ref};$$

$$e_i = e_{i,trans} + e_{i,rot} + e_{i,vib} + e_{i,0};$$

$$h_s = e_i + R_s T. \quad (22)$$

The molecular diffusion terms calculated at the vibrational temperature, $\phi_{v,x}$, $\phi_{v,y}$ and $\phi_{v,z}$, which appear in the vibrational-internal-energy equation are defined by ([11]):

$$\phi_{v,x} = \sum_{s=mol} \rho_s v_{sx} h_{v,s}, \quad \phi_{v,y} = \sum_{s=mol} \rho_s v_{sy} h_{v,s}; \quad (23)$$

$$\phi_{v,z} = \sum_{s=mol} \rho_s v_{sz} h_{v,s}, \quad (24)$$

Table 1. Molecular mass and enthalpy formation of each species.

Species	M (g/g-mol)	$\Delta h_{f,s}$ (J/g-mol)
N	14.0	472,680.0
O	16.0	249,180.0
N ₂	28.0	0.0
O ₂	32.0	0.0
NO	30.0	90,290.0
CO ₂	44.0	-393,510.0
C	12.0	716,680.0
CO	28.0	-110,530.0
CN	26.0	435,100.0

with $h_{v,s}$ being the specific enthalpy (sensible) of the chemical species “s” calculated at the vibrational temperature T_v . The sums of the Eqs. (23-24), as also those present in Eq. (7), considers only the molecules of the system, namely: N₂, O₂,

NO, CO₂, CO and CN.

The molecular mass and the formation enthalpy of each constituent of the Mars atmosphere are given in Tab. 1. Note that to have $\Delta h_{f,s}$ in J/kg, it is only necessary to multiply it by 10^3 and to divide it by the molecular mass.

B. Chemical Model and Reaction Data

The following species are considered for entry into the Martian atmosphere:

N, O, N₂, O₂, NO, CO₂, C, CO, and CN.

These species represent the main constituents of a high temperature mixture of carbon dioxide and nitrogen. The CN molecule is included for assessment purposes though is not expected to be present in large mass fractions. For the moderate entry velocities considered in this work ionization is assumed to be unimportant, thus no ionic species are considered. This chemical model is based on the work of [13]. The reaction set used for these calculations is given in Tab. 2. Reverse reaction rate data are specified directly in Tab. 3. It is assumed that both the forward and reverse reaction rate coefficients have the following Arrhenius temperature dependence:

$$k = AT^\beta e^{-C/T}, \quad (25)$$

Table 2. Reactions and forward coefficients.

Reaction	A	β	C
O ₂ +M \leftrightarrow O+O+M	9.1x10 ¹⁸	-1.0	59,370
N ₂ +M \leftrightarrow N+N+M	2.5x10 ¹⁹	-1.0	113,200
NO+M \leftrightarrow N+O+M	4.1x10 ¹⁸	-1.0	75,330
CO+M \leftrightarrow C+O+M	4.5x10 ¹⁹	-1.0	128,900
CO ₂ +M \leftrightarrow CO+O+M	3.7x10 ¹⁴	0.0	52,500
N ₂ +O \leftrightarrow NO+N	7.4x10 ¹¹	0.5	37,940
NO+O \leftrightarrow O ₂ +N	3.0x10 ¹¹	0.5	19,460
CO+O \leftrightarrow C+O ₂	2.7x10 ¹²	0.5	69,540
CO ₂ +O \leftrightarrow CO+O ₂	1.7x10 ¹³	0.0	26,500
CO+N \leftrightarrow NO+C	2.9x10 ¹¹	0.5	53,630
CN+O \leftrightarrow NO+C	1.6x10 ¹³	0.1	14,600
CO+N \leftrightarrow CN+O	2.0x10 ¹⁴	0.0	38,600
N ₂ +C \leftrightarrow CN+N	2.0x10 ¹⁴	0.0	23,200

where the pre-exponential factor A, the temperature exponent β and the activation energy C are obtained from experiment and are given in Tabs. 2 and 3. M is a third body of collision and can be any species. Data for the forward reactions 1 to 4 and 6 to 10 are taken from [14]. Reaction 5 and 11 to 13 are taken from [15]. Data for the reverse reactions are taken from [14], except for reactions 5 and 9 for which data are from reference [16], and reactions 11 to 13 where data are from [17]. For dissociation reactions the preferential model of Park is used whereby the forward rates are governed by an average

temperature $T_a = \sqrt{T_v T_v}$. With all combinations to M, a total of fifth-three (53) reactions are obtained.

Table 3. Reactions and reverse coefficients.

Reaction	A	β	C
O ₂ +M \leftrightarrow O+O+M	9.0x10 ¹⁵	-0.5	0.0
N ₂ +M \leftrightarrow N+N+M	1.5x10 ¹⁸	-1.0	0.0
NO+M \leftrightarrow N+O+M	3.5x10 ¹⁸	-1.0	0.0
CO+M \leftrightarrow C+O+M	1.0x10 ¹⁸	-1.0	0.0
CO ₂ +M \leftrightarrow CO+O+M	2.4x10 ¹⁵	0.0	2,184
N ₂ +O \leftrightarrow NO+N	1.6x10 ¹¹	0.5	0.0
NO+O \leftrightarrow O ₂ +N	9.5x10 ⁰⁹	1.0	0.0
CO+O \leftrightarrow C+O ₂	9.4x10 ¹²	0.25	0.0
CO ₂ +O \leftrightarrow CO+O ₂	2.5x10 ¹²	0.0	24,000
CO+N \leftrightarrow NO+C	2.6x10 ¹⁰	0.5	0.0
CN+O \leftrightarrow NO+C	3.8x10 ¹²	0.5	4,500
CO+N \leftrightarrow CN+O	6.3x10 ¹¹	0.5	4,500
N ₂ +C \leftrightarrow CN+N	4.4x10 ¹⁴	0.0	4,500

C. Transport Properties

For species N, O, N₂, O₂ and NO curve fits for viscosity as a function of temperature have been developed by [18] which are of the form

$$\mu = 0.1 \times \exp\left[(A_\mu \ln T + B_\mu) \ln T + C_\mu\right]. \quad (26)$$

[19] develops equivalent curve fits for CO and CO₂, while C behaves as O. CN data are from [20]. Data for these curve fits are given in Tab. 4.

Table 4. Coefficients for viscosity curve fits.

Species	A _{μ}	B _{μ}	C _{μ}
N	0.0115572	0.4294404	-12.4327495
O	0.0203144	0.4294404	-11.6031403
N ₂	0.0268142	0.3177838	-11.3155513
O ₂	0.0449290	-0.0826158	-9.2019475
NO	0.0436378	-0.0335511	-9.5767430
CO ₂	-0.0195274	1.0132950	-13.9787300
C	0.0203144	0.4294404	-11.6031403
CO	-0.0195274	1.0478180	-14.3221200
CN	-0.0025000	0.6810000	-12.4914000

The thermal conductivity of translational and rotational energies for each species is derived from species viscosities using an Eucken relation:

$$k_{tr,i} = (5/2 \times c_{v,trans,i} + c_{v,rot,i}), \quad (27)$$

where:

$$c_{v,t} = \begin{cases} 3/2RT, & \text{for molecules} \\ 0.0, & \text{for atoms.} \end{cases} \quad (28)$$

$$c_{v,r} = RT$$

The total viscosity and conductivity of the gas mixture are calculated using the semi-empirical rule of [21]. To the viscosity, for instance:

$$\mu = \sum_{i=1}^{ns} \frac{X_i \mu_i}{\phi_i}, \quad (29)$$

where X_i is the mole fraction of species i and

$$\phi_i = \sum_{j=1}^{ns} \frac{X_j \left[1 + \sqrt{\frac{\mu_i}{\mu_j} \left(\frac{M_j}{M_i} \right)^{1/4}} \right]^2}{\sqrt{8 \left(1 + \frac{M_i}{M_j} \right)}}. \quad (30)$$

X_i can be calculated from

$$X_i = \frac{c_i M}{M_i}, \quad (31)$$

with:

$$M = 1 / \sum_{j=1}^{ns} \frac{c_j}{M_j}; \quad (32)$$

$$c_j = \frac{\rho_j}{\rho} \quad (\text{Mass fraction}). \quad (33)$$

Diffusion coefficients are computed as outlined by [22]. The species diffusion coefficients are calculated from

$$D_i = \frac{M_i (1 - c_i) D}{1 - X_i}. \quad (34)$$

The diffusion coefficient D is calculated from the Schmidt number:

$$S_c = \frac{\mu}{\rho D}. \quad (35)$$

The Schmidt number is set to 0.5 for neutral species and 0.25 for ions.

The species vibrational conductivities are also calculated by the species viscosity and the Eucken formula:

$$k_{v,i} = \mu_i R_i. \quad (36)$$

The vibrational temperature is determined from the definition of the internal vibrational energy of the mixture, on an iterative process, and uses the Newton-Raphson method to find the root, which is merely the approximate vibrational temperature. Three steps are suffices to obtain a good approximation.

D. Source Terms

The source terms for the species mass fractions in the chemically reacting flow are giving by:

$$\dot{\omega}_i = M_i \sum_{r=1}^{nr} (v_{i,r}'' - v_{i,r}') \times \left\{ k_{f,i} \prod_{j=1}^{j_{\max}} (\rho_j / M_j)^{v_{j,r}'} - k_{r,i} \prod_{j=1}^{j_{\max}} (\rho_j / M_j)^{v_{j,r}''} \right\}. \quad (37)$$

The reaction rate coefficients k_f and k_r are calculated as a function of a rate controlling temperature T_a , as given in section B.

E. Vibrational Relaxation Model

The vibrational internal energy of a molecule, in J/kg, is defined by:

$$e_{v,s} = \frac{R_s \theta_{v,s}}{e^{\theta_{v,s}/T_v} - 1}, \quad (38)$$

and the vibrational internal energy of all molecules is given by:

$$e_v = \sum_{s=\text{mol}} c_s e_{v,s}. \quad (39)$$

The heat flux due to translational-vibrational relaxation, according to [23], is given by:

$$q_{T-v,s} = \rho_s \frac{e_{v,s}^*(T) - e_{v,s}(T_v)}{\tau_s}, \quad (40)$$

where: $e_{v,s}^*$ is the vibrational internal energy calculated at the translational temperature to the species "s"; and τ_s is the translational-vibrational relaxation time to the molecular species, in s. The relaxation time is the time of energy exchange between the translational and vibrational molecular modes.

Vibrational characteristic time of [24]. According to [25], the relaxation time of molar average of [24] is described by:

$$\tau_s = \tau_s^{M-W} = \sum_{l=1}^{ns} X_l / \sum_{l=1}^{ns} X_l / \tau_{s,l}^{M-W}, \quad (41)$$

with:

$\tau_{s,l}^{M-W}$ is the relaxation time between species of [24];
 τ_s^{M-W} is the vibrational characteristic time of [24];
 $X_l = c_l / (N_{AV} m_l)$ and $m_l = M_l / N_{AV}$.

$$(42)$$

Definition of $\tau_{s,l}^{M-W}$. For temperatures inferior to or equal to 8,000 K, [24] give the following semi-empirical correlation to the vibrational relaxation time due to inelastic collisions:

$$\tau_{s,l}^{M-W} = \left(\frac{B}{p_l} \right) e^{[A_{s,l}(T^{-1/3} - 0.015\mu_{s,l}^{1/4}) - 18.42]}, \quad (43)$$

where:

$B = 1.013 \times 10^5 \text{Ns/m}^2$ ([26]);
 p_l is the partial pressure of species “l” in N/m^2 ;
 $A_{s,l} = 1.16 \times 10^{-3} \mu_{s,l}^{1/2} \theta_{v,s}^{4/3}$ ([26]);

$$(44)$$

$$\mu_{s,l} = \frac{M_s M_l}{M_s + M_l}, \quad (45)$$

being the reduced molecular mass of the collision partners: kg/kg-mol ;

T and $\theta_{v,s}$ in Kelvin.

The values of the characteristic vibrational temperature are given in Tab. 5. In the absence of specific vibrational relaxation data for CN the molecule has been assumed to behave as CO.

Table 5. Vibrational energy constants.

Species	θ_v (K)
N ₂	3395.0
O ₂	2239.0
NO	2817.0
CO	3074.0
CN	3074.0

[27] correction time. For temperatures superiors to 8,000 K, the Eq. (43) gives relaxation times less than those observed in experiments. To temperatures above 8,000 K, [27] suggests the following relation to the vibrational relaxation time:

$$\tau_s^P = \frac{1}{\xi_s \sigma_v n_s}, \quad (46)$$

where:

$$\xi_s = \sqrt{\frac{8R_s T}{\pi}}, \quad (47)$$

being the molecular average velocity in m/s ;

$$\sigma_v = 10^{-20} \left(\frac{50,000}{T} \right)^2, \quad (48)$$

being the effective collision cross-section to vibrational relaxation in m^2 ; and

$$n_s = \rho_s / m_s, \quad (49)$$

being the density of the number of collision particles of species “s”. ρ_s in kg/m^3 and m_s in kg/particle , defined by Eq. (42).

Combining the two relations, the following expression to the vibrational relaxation time is obtained:

$$\tau_s = \tau_s^{M-W} + \tau_s^P. \quad (50)$$

[27] emphasizes that this expression [Eq. (50)] to the vibrational relaxation time is applicable to a range of temperatures much more vast.

III. STRUCTURED VAN LEER AND LIU AND STEFFEN JR. ALGORITHMS TO THERMOCHEMICAL NON-EQUILIBRIUM

As shown in [8], the discrete convective flux calculated by the AUSM scheme (“Advection Upstream Splitting Method”) can be interpreted as a sum involving the arithmetical average between the right (R) and the left (L) states of the $(i+1/2,j,k)$ cell face, related to cell (i,j,k) and its $(i+1,j,k)$ neighbour, respectively, multiplied by the interface Mach number, and a scalar dissipative term. [28] have suggested that the flux integrals could be calculated defining each part, dynamic, chemical and vibrational, separately. Hence, to the $(i+1/2,j,k)$ interface, considering the dynamical part of the formulation:

$$R_{i+1/2,j,k} = |S_{i+1/2,j,k}| \left\{ \frac{1}{2} M_{i+1/2,j,k} \left[\begin{matrix} \rho a \\ \rho a u \\ \rho a v \\ \rho a w \\ \rho a H \end{matrix} \right]_L + \begin{matrix} \rho a \\ \rho a u \\ \rho a v \\ \rho a w \\ \rho a H \end{matrix} \right]_R \right\} - \frac{1}{2} \phi_{i+1/2,j,k} \left[\begin{matrix} \rho a \\ \rho a u \\ \rho a v \\ \rho a w \\ \rho a H \end{matrix} \right]_R - \left[\begin{matrix} \rho a \\ \rho a u \\ \rho a v \\ \rho a w \\ \rho a H \end{matrix} \right]_L \right\} + \begin{matrix} 0 \\ S_x p \\ S_y p \\ S_z p \\ 0 \end{matrix} \Big|_{i+1/2,j,k}. \quad (51)$$

The components of the unity vector normal to the flux interface, the flux area of each interface and the cell volume are defined in [6; 29].

The “a” quantity represents the frozen speed of sound. $M_{i+1/2,j,k}$ defines the advection Mach number at the

($i+1/2,j,k$) face of the (i,j,k) cell, which is calculated according to [8] as:

$$M_i = M_L^+ + M_R^-, \quad (52)$$

where the separated Mach numbers M^{\pm} are defined by the [3] formulas:

$$M^+ = \begin{cases} M, & \text{if } M \geq 1; \\ 0.25(M+1)^2, & \text{if } |M| < 1; \\ 0, & \text{if } M \leq -1; \end{cases}$$

$$M^- = \begin{cases} 0, & \text{if } M \geq 1; \\ -0.25(M-1)^2, & \text{if } |M| < 1; \\ M, & \text{if } M \leq -1. \end{cases} \quad (53)$$

M_L and M_R represent the Mach number associated with the left and right states, respectively. The advection Mach number is defined by:

$$M = (S_x u + S_y v + S_z w) / (|S|a). \quad (54)$$

The pressure at the ($i+1/2,j,k$) face of the (i,j,k) cell is calculated by a similar way:

$$p_i = p_L^+ + p_R^-, \quad (55)$$

with p^{\pm} denoting the pressure separation defined according to the [3] formulas:

$$p^+ = \begin{cases} p, & \text{if } M \geq 1; \\ 0.25p(M+1)^2(2-M), & \text{if } |M| < 1; \\ 0, & \text{if } M \leq -1; \end{cases}$$

$$p^- = \begin{cases} 0, & \text{if } M \geq 1; \\ 0.25p(M-1)^2(2+M), & \text{if } |M| < 1; \\ p, & \text{if } M \leq -1. \end{cases} \quad (56)$$

The definition of the dissipative term ϕ determines the particular formulation of the convective fluxes. According to [30], the choice below corresponds to the [3] scheme:

$$\phi_{i+1/2,j,k} = \begin{cases} |M_{i+1/2,j,k}|, & \text{if } |M_{i+1/2,j,k}| \geq 1; \\ |M_{i+1/2,j,k}| + 0.5(M_R - 1)^2, & \text{if } 0 \leq M_{i+1/2,j,k} < 1; \\ |M_{i+1/2,j,k}| + 0.5(M_L + 1)^2, & \text{if } -1 < M_{i+1/2,j,k} \leq 0; \end{cases} \quad (57)$$

and the choice below corresponds to the [8] scheme:

$$\phi_{i+1/2,j,k} = |M_{i+1/2,j,k}|; \quad (58)$$

the discrete-chemical-convective flux is defined by:

$$R_{i+1/2,j,k} = |S|_{i+1/2,j,k} \left\{ \frac{1}{2} M_{i+1/2,j,k} \left[\begin{array}{c} \left(\begin{array}{c} \rho_1 a \\ \rho_2 a \\ \rho_3 a \\ \rho_4 a \\ \rho_5 a \\ \rho_7 a \\ \rho_8 a \\ \rho_9 a \end{array} \right)_L \\ + \\ \left(\begin{array}{c} \rho_1 a \\ \rho_2 a \\ \rho_3 a \\ \rho_4 a \\ \rho_5 a \\ \rho_7 a \\ \rho_8 a \\ \rho_9 a \end{array} \right)_R \end{array} \right] \right. \\ \left. - \frac{1}{2} \phi_{i+1/2,j,k} \left[\begin{array}{c} \left(\begin{array}{c} \rho_1 a \\ \rho_2 a \\ \rho_3 a \\ \rho_4 a \\ \rho_5 a \\ \rho_7 a \\ \rho_8 a \\ \rho_9 a \end{array} \right)_R \\ - \\ \left(\begin{array}{c} \rho_1 a \\ \rho_2 a \\ \rho_3 a \\ \rho_4 a \\ \rho_5 a \\ \rho_7 a \\ \rho_8 a \\ \rho_9 a \end{array} \right)_L \end{array} \right] \right\}, \quad (59)$$

and the discrete-vibrational-convective flux is determined by:

$$R_{i+1/2,j,k} = |S|_{i+1/2,j,k} \left\{ \frac{1}{2} M_{i+1/2,j,k} [(\rho e_v a)_L + (\rho e_v a)_R] \right. \\ \left. - \frac{1}{2} \phi_{i+1/2,j,k} [(\rho e_v a)_R - (\rho e_v a)_L] \right\}. \quad (60)$$

The time integration is performed employing the Runge-Kutta explicit method of five stages, second-order accurate, to the three types of convective flux.

To the dynamic part, this method can be represented in general form by:

$$Q_{i,j,k}^{(0)} = Q_{i,j,k}^{(n)}$$

$$Q_{i,j,k}^{(k)} = Q_{i,j,k}^{(0)} - \alpha_k \Delta t_{i,j,k} R(Q_{i,j,k}^{(k-1)}) / V_{i,j,k}, \quad (61)$$

$$Q_{i,j,k}^{(n+1)} = Q_{i,j,k}^{(k)}$$

to the chemical part, it can be represented in general form by:

$$Q_{i,j,k}^{(0)} = Q_{i,j,k}^{(n)}$$

$$Q_{i,j,k}^{(m)} = Q_{i,j,k}^{(0)} - \alpha_m \Delta t_{i,j,k} [R(Q_{i,j,k}^{(m-1)}) / V_{i,j,k} - S_C(Q_{i,j,k}^{(m-1)})], \quad (62)$$

$$Q_{i,j,k}^{(n+1)} = Q_{i,j,k}^{(m)}$$

where the chemical source term S_C is calculated with the temperature T_a . Finally, to the vibrational part:

$$\begin{aligned}
 Q_{i,j,k}^{(0)} &= Q_{i,j,k}^{(n)} \\
 Q_{i,j,k}^{(m)} &= Q_{i,j,k}^{(0)} - \alpha_m \Delta t_{i,j,k} \left[R(Q_{i,j,k}^{(m-1)}) / V_{i,j,k} - S_v(Q_{i,j,k}^{(m-1)}) \right], \quad (63) \\
 Q_{i,j,k}^{(n+1)} &= Q_{i,j,k}^{(m)}
 \end{aligned}$$

in which:

$$S_v = \sum_{s=\text{mol}} q_{T-v,s} + \sum_{s=\text{mol}} S_{C,s} e_{v,s}; \quad (64)$$

$m = 1, \dots, 5$; $\alpha_1 = 1/4$, $\alpha_2 = 1/6$, $\alpha_3 = 3/8$, $\alpha_4 = 1/2$ and $\alpha_5 = 1$. This scheme is first-order accurate in space and second-order accurate in time. The second-order of spatial accuracy is obtained by the ‘‘MUSCL’’ procedure.

The viscous formulation follows that of [31], which adopts the Green theorem to calculate primitive variable gradients. The viscous vectors are obtained by arithmetical average between cell (i,j,k) and its neighbours. As was done with the convective terms, there is a need to separate the viscous flux in three parts: dynamical viscous flux, chemical viscous flux and vibrational viscous flux. The dynamical part corresponds to the first five equations of the Navier-Stokes ones, the chemical part corresponds to the following eight equations and the vibrational part corresponds to the last equation.

IV. MUSCL PROCEDURE

Second order spatial accuracy can be achieved by introducing more upwind points or cells in the schemes. It has been noted that the projection stage, whereby the solution is projected in each cell face (i-1/2,j,k; i+1/2,j,k) on piecewise constant states, is the cause of the first order space accuracy of the Godunov schemes ([10]). Hence, it is sufficient to modify the first projection stage without modifying the Riemann solver, in order to generate higher spatial approximations. The state variables at the interfaces are thereby obtained from an extrapolation between neighboring cell averages. This method for the generation of second order upwind schemes based on variable extrapolation is often referred to in the literature as the MUSCL approach. The use of nonlinear limiters in such procedure, with the intention of restricting the amplitude of the gradients appearing in the solution, avoiding thus the formation of new extrema, allows that first order upwind schemes be transformed in TVD high resolution schemes with the appropriate definition of such nonlinear limiters, assuring monotone preserving and total variation diminishing methods. Details of the present implementation of the MUSCL procedure, as well the incorporation of TVD properties to the schemes, are found in [10]. The expressions to calculate the fluxes following a MUSCL procedure and the nonlinear flux limiter definitions employed in this work, which incorporates TVD properties, are defined as follows.

The conserved variables at the interface (i+1/2,j,k) can be considered as resulting from a combination of backward and forward extrapolations. To a linear one-sided extrapolation at the interface between the averaged values at the two upstream

cells (i,j,k) and (i+1,j,k), one has:

$$Q_{i+1/2,j,k}^L = Q_{i,j,k} + \frac{\varepsilon}{2} (Q_{i,j,k} - Q_{i-1,j,k}), \quad \text{cell (i,j,k);} \quad (65)$$

$$Q_{i+1/2,j,k}^R = Q_{i+1,j,k} - \frac{\varepsilon}{2} (Q_{i+2,j,k} - Q_{i+1,j,k}), \quad \text{cell (i+1,j,k),} \quad (66)$$

leading to a second order fully one-sided scheme. If the first order scheme is defined by the numerical flux

$$F_{i+1/2,j,k} = F(Q_{i,j,k}, Q_{i+1,j,k}) \quad (67)$$

the second order space accurate numerical flux is obtained from

$$F_{i+1/2,j,k}^{(2)} = F(Q_{i+1/2,j,k}^L, Q_{i+1/2,j,k}^R). \quad (68)$$

Higher order flux vector splitting methods, such as those studied in this work, are obtained from:

$$F_{i+1/2,j,k}^{(2)} = F^+(Q_{i+1/2,j,k}^L) + F^-(Q_{i+1/2,j,k}^R). \quad (69)$$

All second order upwind schemes necessarily involve at least five mesh points or cells.

To reach high order solutions without oscillations around discontinuities, nonlinear limiters are employed, replacing the term ε in Eqs. (65) and (66) by these limiters evaluated at the left and at the right states of the flux interface. To define such limiters, it is necessary to calculate the ratio of consecutive variations of the conserved variables. These ratios are defined as follows:

$$\begin{aligned}
 r_{i-1/2,j,k}^+ &= (Q_{i+1,j,k} - Q_{i,j,k}) / (Q_{i,j,k} - Q_{i-1,j,k}) \\
 r_{i+1/2,j,k}^+ &= (Q_{i+2,j,k} - Q_{i+1,j,k}) / (Q_{i+1,j,k} - Q_{i,j,k}), \quad (70)
 \end{aligned}$$

where the nonlinear limiters at the left and at the right states of the flux interface are defined by $\Psi^L = \Psi(r_{i-1/2,j,k}^+)$ and $\Psi^R = \Psi(1/r_{i+1/2,j,k}^+)$. In this work, five options of nonlinear limiters were considered to the numerical experiments. These limiters are defined as follows:

$$\Psi_1^{VL}(r_1) = \frac{r_1 + |r_1|}{1 + r_1}, \quad \text{[32] limiter;} \quad (71)$$

$$\Psi_1^{VA}(r_1) = \frac{r_1 + r_1^2}{1 + r_1^2}, \quad \text{Van Albada limiter;} \quad (72)$$

$$\Psi_1^{MIN}(r_1) = \text{signal}_1 \text{MAX}(0, \text{MIN}(|r_1|, \text{signal}_1)), \quad \text{minmod limiter;} \quad (73)$$

$$\Psi_1^{SB}(r_1) = \text{MAX}(0, \text{MIN}(2r_1, 1), \text{MIN}(r_1, 2)), \quad \text{‘‘Super Bee’’}$$

limiter, due to [33]; (74)

$$\Psi_1^{\beta-L}(r_1) = \text{MAX}(0, \text{MIN}(\beta r_1, 1), \text{MIN}(r_1, \beta)), \beta\text{-limiter,} \quad (75)$$

with “l” varying from 1 to 14 (three-dimensional space), signal being equal to 1.0 if $r_1 \geq 0.0$ and -1.0 otherwise, r_1 is the ratio of consecutive variations of the lth conserved variable and β is a parameter assuming values between 1.0 and 2.0, being 1.5 the value assumed in this work.

With the implementation of the numerical flux vectors following this MUSCL procedure, second order spatial accuracy and TVD properties are incorporated in the algorithms.

V. DEGENERACY OF CO₂, VIBRATIONAL ENERGY, FROZEN SPEED OF SOUND AND TOTAL ENERGY EQUATION

The CO₂ presents three levels of degeneracy, each one corresponding to a characteristic vibrational mode. The characteristic vibrational temperature and the respective degeneracy weights are given in Tab. 6.

Table 6. Values of g’s and θ_v ’s.

Degeneracy	g	θ_v
1	1	1,903.0
2	2	945.0
3	1	3,329.0

Hence, the vibrational energy is determined by:

$$e_v = \sum_{s=1}^{ns} c_s e_{v,s} = \sum_{\substack{s=1 \\ s \neq 6}}^{ns} c_s e_{v,s} + g_1 c_{CO_2} e_{v,1} + g_2 c_{CO_2} e_{v,2} + g_3 c_{CO_2} e_{v,3}, \quad (76)$$

with e_v given by Eq. (39). The frozen speed of sound is given by the following equation:

$$\beta = \frac{R\sigma}{\rho c_{v,mix}} \quad \text{and} \quad a = \sqrt{\frac{(1+\beta)p}{\rho}}, \quad (77)$$

with:

R being the universal gas constant;

$$\sigma = \sum_{s=1}^{ns} \frac{\rho_s}{M_s}; \quad (78)$$

$$c_{v,mix} = \sum_{s=1}^{ns} c_s c_{v,s}, \quad (79)$$

$c_{v,s}$ being the specific heat at constant volume for each species. The total energy is given by:

$$e = \rho \left[c_{v,mix} T + (\Delta h_{f,mix} - R_{mix} T_{ref}) + e_v + \frac{1}{2} (u^2 + v^2 + w^2) \right], \quad (80)$$

where:

$$\Delta h_{f,mix} = \sum_{s=1}^{ns} c_s \Delta h_{f,s}; \quad (81)$$

$$R_{mix} = \sum_{s=1}^{ns} c_s R_s; \quad (82)$$

$$T_{ref} = 298.15K.$$

VI. INITIAL AND BOUNDARY CONDITIONS

A. Initial Condition

As initial conditions, the following flow properties are given: ρ_{init} , u_{init} , α , $T_{tr,init}$, $T_{v,init}$, $c_s(1)$, $c_s(2)$, $c_s(3)$, $c_s(4)$, $c_s(5)$, $c_s(7)$, $c_s(8)$, and $c_s(9)$, in which: α is the flow attack angle, $T_{tr,init}$ is the initial translational/rotational temperature, $T_{v,init}$ is the initial vibrational temperature, and the c_s ’s are the initial mass fractions of the N, O, N₂, O₂, NO, C, CO and CN. In this way, the $c_s(6)$ is easily obtained from:

$$c_s(6) = 1 - \sum_{\substack{s=1 \\ s \neq 6}}^{ns} c_s \quad (83)$$

Initially, $T_{v,init} = T_{tr,init}$. The dimensionless variables which will compose the initial vector of conserved variables are determined as follows:

$$\rho_{dim} = \rho_{init}/\rho_\infty, \quad u_{dim} = u_{init}/a_{char}, \quad v_{dim} = v_{init}/a_{char}, \quad T_{tr,dim} = T_{tr,init}/a_{char} \quad \text{and} \quad T_{v,dim} = T_{v,init}/a_{char}, \quad (84)$$

with:

ρ_∞ defining the freestream density;

α is the flow attack angle;

a_{char} obtained from tables of the Mars atmosphere properties.

Considering the species mass fractions and with the values of the species specific heat at constant volume, it is possible to obtain the mixture specific heat at constant volume. The mixture formation enthalpy is also obtained from the mass fractions and from the species formation enthalpies. The dimensionless internal vibrational energy to each species is obtained from:

$$e_{v,dim,N_2} = R_{N_2} \theta_{v,N_2} / \left\{ e^{\left[\theta_{v,N_2} / T_{v,dim} \right]} - 1 \right\};$$

$$e_{v,dim,O_2} = R_{O_2} \theta_{v,O_2} / \left\{ e^{\left[\theta_{v,O_2} / T_{v,dim} \right]} - 1 \right\};$$

$$e_{v,dim,NO} = R_{NO} \theta_{v,NO} / \left\{ e^{\left[\theta_{v,NO} / T_{v,dim} \right]} - 1 \right\};$$

$$\begin{aligned}
e_{v,\text{dim},\text{CO}_2(1)} &= g(1) \times R_{\text{CO}_2} \theta_{v,\text{CO}_2(1)} / \left\{ e^{\left[\theta_{v,\text{CO}_2(1)} / T_{v,\text{dim}} \right] - 1} \right\}; \\
e_{v,\text{dim},\text{CO}_2(2)} &= g(2) \times R_{\text{CO}_2} \theta_{v,\text{CO}_2(2)} / \left\{ e^{\left[\theta_{v,\text{CO}_2(2)} / T_{v,\text{dim}} \right] - 1} \right\}; \\
e_{v,\text{dim},\text{CO}_2(3)} &= g(3) \times R_{\text{CO}_2} \theta_{v,\text{CO}_2(3)} / \left\{ e^{\left[\theta_{v,\text{CO}_2(3)} / T_{v,\text{dim}} \right] - 1} \right\}; \\
e_{v,\text{dim},\text{CO}} &= R_{\text{CO}} \theta_{v,\text{CO}} / \left\{ e^{\left[\theta_{v,\text{CO}} / T_{v,\text{dim}} \right] - 1} \right\}; \\
e_{v,\text{dim},\text{CN}} &= R_{\text{CN}} \theta_{v,\text{CN}} / \left\{ e^{\left[\theta_{v,\text{CN}} / T_{v,\text{dim}} \right] - 1} \right\}. \quad (85)
\end{aligned}$$

The total internal vibrational energy of the system is determined by Eq. (39). Finally, the dimensionless total energy is determined by Eq. (80). The initial vector of conserved variables is, therefore, defined by:

$$\mathbf{Q} = \left\{ \begin{array}{l} \rho_{\text{dim}} \\ \rho_{\text{dim}} \mathbf{u}_{\text{dim}} \\ \rho_{\text{dim}} v_{\text{dim}} \\ \rho_{\text{dim}} \mathbf{w}_{\text{dim}} \\ e_{\text{dim}} \\ \rho_{\text{dim}} c_s(1) \\ \rho_{\text{dim}} c_s(2) \\ \rho_{\text{dim}} c_s(3) \\ \rho_{\text{dim}} c_s(4) \\ \rho_{\text{dim}} c_s(5) \\ \rho_{\text{dim}} c_s(7) \\ \rho_{\text{dim}} c_s(8) \\ \rho_{\text{dim}} c_s(9) \\ \rho_{\text{dim}} e_{v,\text{dim}} \end{array} \right\}. \quad (86)$$

B. Boundary Conditions

(a) Dynamical Part:

The boundary conditions are basically of three types: solid wall, entrance and exit. These conditions are implemented in special cells, named ghost cell.

(a.1) Wall condition: To inviscid flow, this condition imposes the flow tangency at the solid wall. This condition is satisfied considering the wall tangent velocity component of the ghost volume as equals to the respective velocity component of its real neighbor cell. At the same way, the wall normal velocity component of the ghost cell is equaled in value, but with opposite signal, to the respective velocity component of the real neighbor cell. It results in:

$$u_g = (1 - 2n_x^2)u_r + (-2n_x n_y)v_r + (-2n_x n_z)w_r; \quad (87)$$

$$v_g = (-2n_y n_x)u_r + (1 - 2n_y^2)v_r + (-2n_y n_z)w_r; \quad (88)$$

$$w_g = (-2n_z n_x)u_r + (-2n_z n_y)v_r + (1 - 2n_z^2)w_r; \quad (89)$$

with “g” related with ghost cell and “r” related with real cell.

To the viscous case, the boundary condition imposes that the ghost cell velocity components be equal to the real cell velocity components, with the negative signal:

$$u_f = -u_r, \quad v_f = -v_r \quad \text{and} \quad w_f = -w_r. \quad (90)$$

The pressure gradient normal to the wall is assumed be equal to zero, following an inviscid formulation and according to the boundary layer theory. The same hypothesis is applied to the temperature gradient normal to the wall, considering adiabatic wall. The ghost volume density and pressure are extrapolated from the respective values of the real neighbor volume (zero order extrapolation), with these two conditions. The total energy is obtained by the state equation of a perfect gas.

(a.2) Entrance condition:

(a.2.1) Subsonic flow: Four properties are specified and one is extrapolated, based on analysis of information propagation along characteristic directions in the calculation domain ([34]). In other words, four characteristic directions of information propagation point inward the computational domain and should be specified. Only the characteristic direction associated to the “(qn-a)” velocity cannot be specified and should be determined by interior information of the calculation domain. The total energy was the extrapolated variable from the real neighbor volume, to the studied problems. Density and velocity components had their values determined by the initial flow properties.

(a.2.2) Supersonic flow: All variables are fixed with their initial flow values.

(a.3) Exit condition:

(a.3.1) Subsonic flow: Four characteristic directions of information propagation point outward the computational domain and should be extrapolated from interior information ([34]). The characteristic direction associated to the “(qn-a)” velocity should be specified because it penetrates the calculation domain. In this case, the ghost volume’s total energy is specified by its initial value. Density and velocity components are extrapolated.

(a.3.2) Supersonic flow: All variables are extrapolated from the interior domain due to the fact that all five characteristic directions of information propagation of the Euler equations point outward the calculation domain and, with it, nothing can be fixed.

(b) Chemical Part:

The boundary conditions to the chemical part are also of three types: solid wall, entrance and exit.

(b.1) Wall condition: In both inviscid and viscous cases, the non-catalytic wall condition is imposed, which corresponds to a zero order extrapolation of the species density from the neighbor real cells.

(b.2) Entrance condition: In this case, the species densities of

each ghost cell are fixed with their initial values (freestream values).

(b.3) Exit condition: In this case, the species densities are extrapolated from the values of the neighbor real cells.

(c) Vibrational Part:

The boundary conditions in the vibrational part are also of three types: solid wall, entrance and exit.

(c.1) Wall condition: In both inviscid and viscous cases, the internal vibrational energy of the ghost cell is extrapolated from the value of its neighbor real cell.

(c.2) Entrance condition: In this case, the internal vibrational energy of each ghost cell is fixed with its initial value (freestream value).

(c.3) Exit condition: In this case, the internal vibrational energy is extrapolated from the value of the neighbor real cell.

VII. SPATIALLY VARIABLE TIME STEP

The basic idea of this procedure consists in keeping constant the CFL number in all calculation domain, allowing, hence, the use of appropriated time steps to each specific mesh region during the convergence process. According to the definition of the CFL number, it is possible to write:

$$\Delta t_{i,j,k} = \text{CFL}(\Delta s)_{i,j,k} / c_{i,j,k}, \quad (83)$$

where CFL is the ‘‘Courant-Friedrichs-Lewy’’ number to provide numerical stability to the scheme; $c_{i,j,k} = \left[(u^2 + v^2)^{0.5} + a \right]_{i,j,k}$ is the maximum characteristic speed of information propagation in the calculation domain; and $(\Delta s)_{i,j,k}$ is a characteristic length of information transport. On a finite volume context, $(\Delta s)_{i,j,k}$ is chosen as the minor value found between the minor baricenter distance, involving the (i,j,k) cell and a neighbor, and the minor cell side length.

VIII. CONFIGURATIONS AND EMPLOYED MESHES

Figures 1 and 2 present the employed meshes to the structured simulations in three-dimensions for the reactive flow around the blunt body. Figure 1 shows the structured mesh to inviscid simulations, whereas Fig. 2 presents the structured mesh to viscous simulations. The viscous case mesh exhibits an exponential stretching in the η direction with a value of 7.5%. The inviscid case mesh has 33,984 hexahedral cells and 39,000 nodes, which corresponds in finite differences to a mesh of 65x60x10 points. The viscous case mesh has the same number of hexahedral cells and nodes.

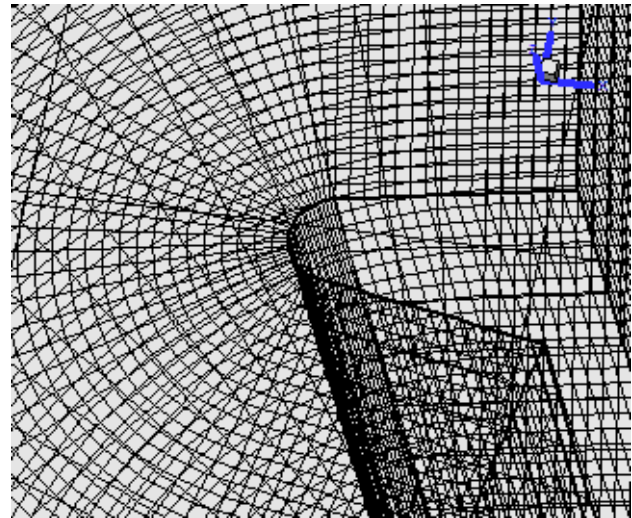


Figure 1. 3D structured mesh for inviscid flow.

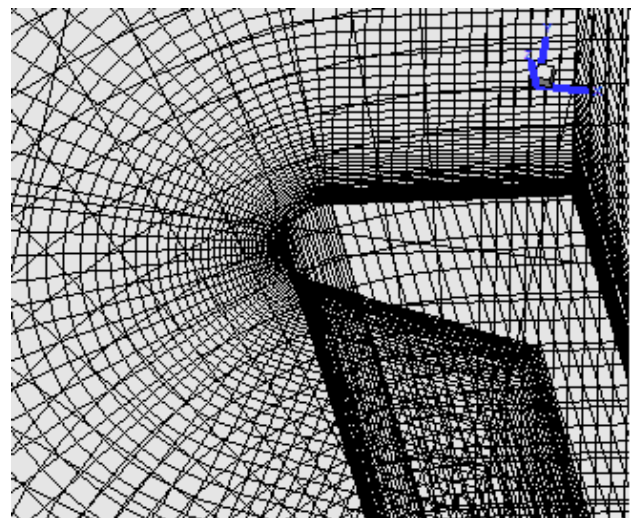


Figure 2. 3D structured mesh for viscous flow.

IX. RESULTS

Tests were performed in a notebook with INTEL Core i7 processor of 2.0GHz and 8GBytes of RAM memory. As the interest of this work is steady state problems, it is necessary to define a criterion which guarantees the convergence of the numerical results. The criterion adopted was to consider a reduction of no minimal three (3) orders of magnitude in the value of the maximum residual in the calculation domain, a typical CFD-community criterion. In the simulations, the attack angle was set equal to zero.

A. Blunt Body Problem

The initial conditions are presented in Tab. 7. The Reynolds number is obtained from data available in the Mars atmosphere tables [35]. The geometry of this problem is a blunt body with 0.85m of nose radius and rectilinear walls with 10° inclination. The far field is located at 20.0 times the nose radius in relation to the configuration nose.

Table 7. Initial conditions to the blunt body problem.

Property	Value
M_∞	31.0
ρ_∞	0.0002687 kg/m ³
p_∞	8.3039 Pa
U_∞	6,155 m/s
T_∞	160.9 K
Altitude	41,700 m
c_N	0.00
c_O	0.00
c_{N_2}	0.03
c_{O_2}	0.00
c_{NO}	0.00
c_{CO_2}	0.97
c_C	0.00
c_{CO}	0.00
c_{CN}	0.00
L	1.7 m
Re_∞	3.23×10^5

Inviscid, first order, structured results. Figures 3 and 4 exhibit the pressure contours obtained by the [3] and the [8] schemes, respectively. As can be observed, the [8] pressure field is more severe than the [3] pressure field. Good symmetry characteristics are observed in both figures.

Figures 7 and 8 show the translational / rotational temperature contours obtained by the [3] and the [8] schemes, respectively. As can be observed, the temperatures are very high in comparison with the temperatures observed in reentry flows in Earth ([6]). The [3] scheme captures a temperature peak of 20,839K, whereas the [8] scheme captures a temperature peak of 22,962K. Hence, the [8] algorithm captures a more severe temperature field.

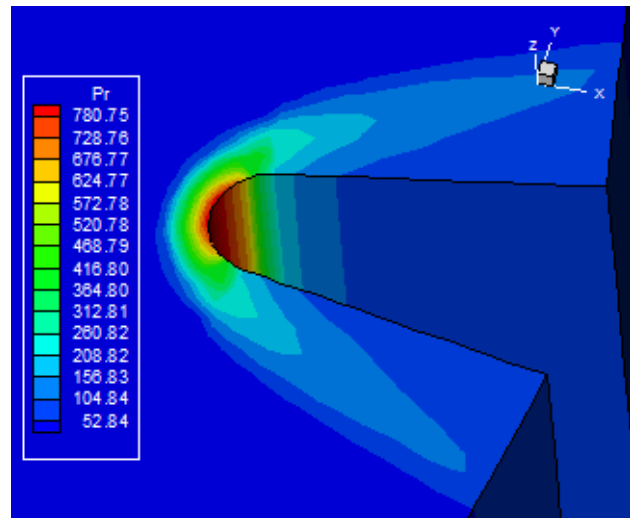


Figure 4. Pressure contours ([8]).

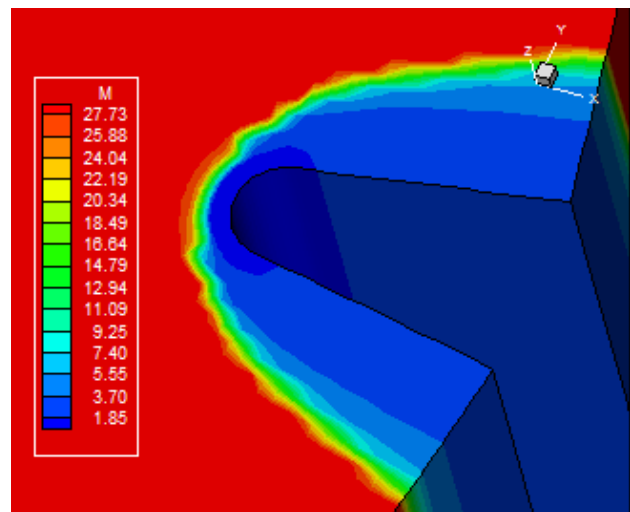


Figure 5. Mach number contours ([3]).

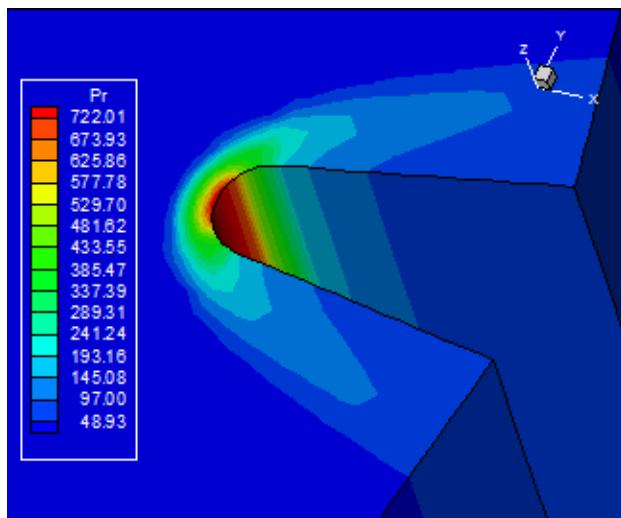


Figure 3. Pressure contours ([3]).

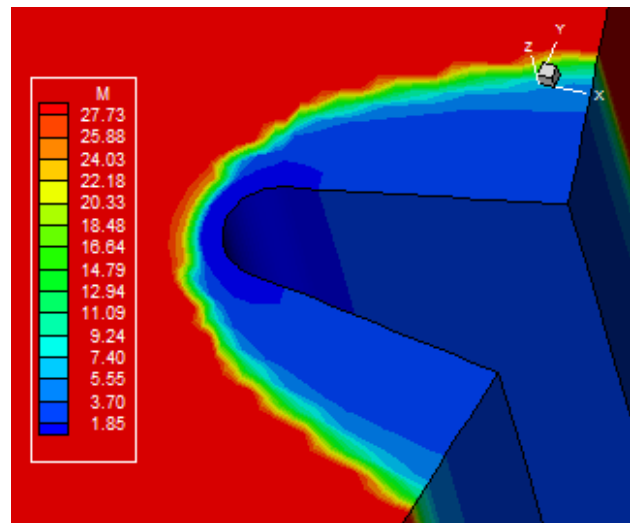


Figure 6. Mach number contours ([8]).

Figures 5 and 6 present the Mach number contours captured by the [3] and the [8] algorithms, respectively. Good symmetry properties are observed in both figures. The Mach

number field captured by the [3] scheme is more severe than that captured by the [8] scheme. Both peaks are very high and an appropriate thermal protection is necessary to guarantee the integrity of the spatial vehicle. This thermal protection should be located mainly in the blunt nose, which receives the main contribution of the heating. To this range of temperature, the main heating contribution is due to radiation and a blunt slender profile is recommended to reduce such effect, as was used in this example.

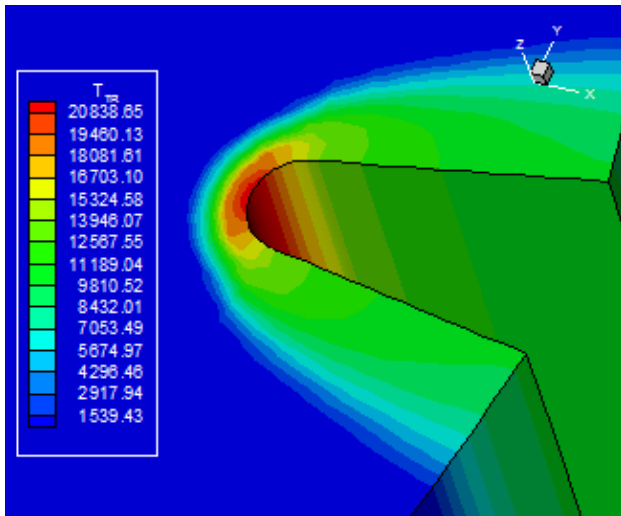


Figure 7. Translational/rotational temperature contours ([3]).

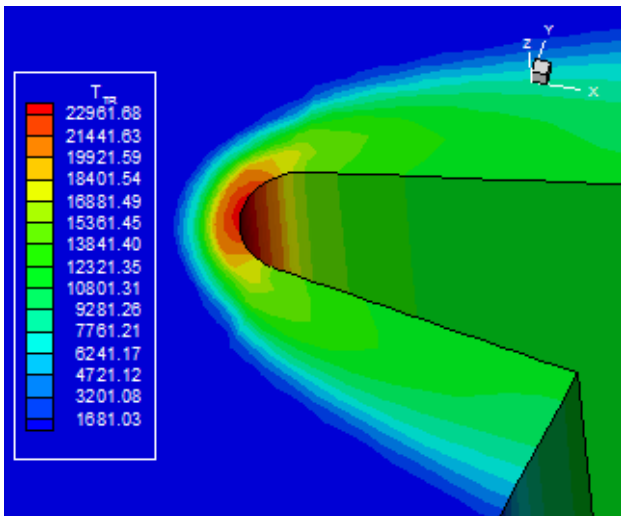


Figure 8. Translational/rotational temperature contours ([8]).

Figures 9 and 10 exhibit the vibrational temperature contours captured by the [3] and the [8] schemes, respectively. As can be seen, the most severe vibrational temperature field is presented by the [8] solution. The solution presented by the [3] scheme is less intense than the [8] solution. Moreover, the [3] solution is smoother, whereas the [8] solution presents wiggles close to the inclined walls/blunt nose interface regions.

Figure 11 shows the mass fraction distributions at the stagnation line of the blunt body, generated by the [3] algorithm. As can be seen, a discrete dissociation of CO_2 occurs, with discrete formation of CO.

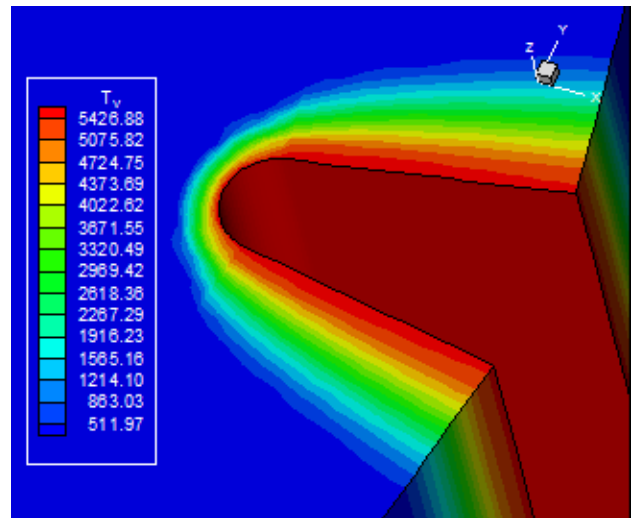


Figure 9. Vibrational temperature contours ([3]).

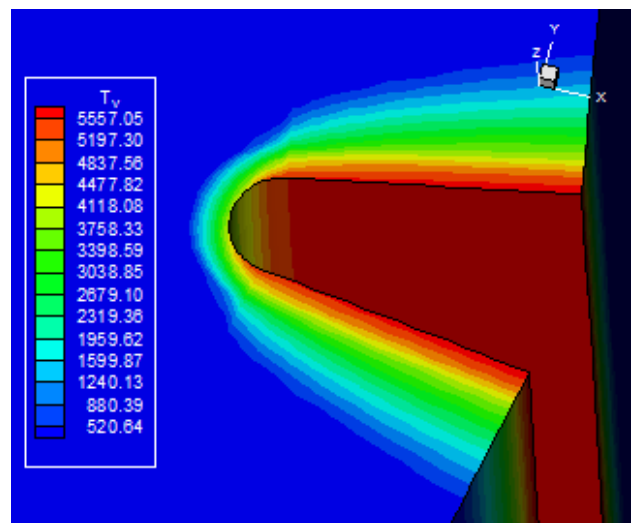


Figure 10. Vibrational temperature contours ([8]).

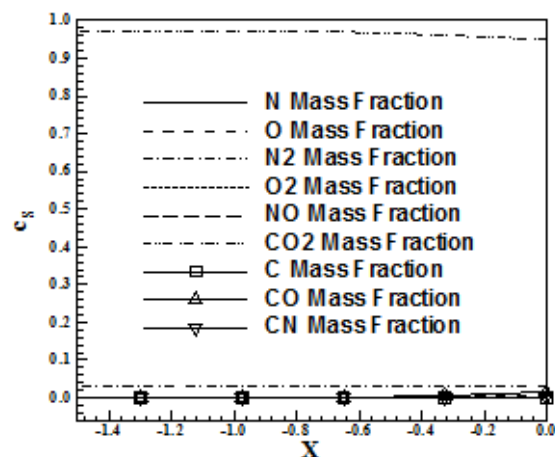


Figure 11. Mass fraction distributions at the stagnation line ([3]).

Figure 12 presents the mass fraction distributions of the nine species along the body stagnation line, generated by the [8] algorithm. As in [3] solution, a discrete CO_2 dissociation

occurs close to the body. The formation of CO, in relation to the [3] solution, is more discrete, almost indistinguishable

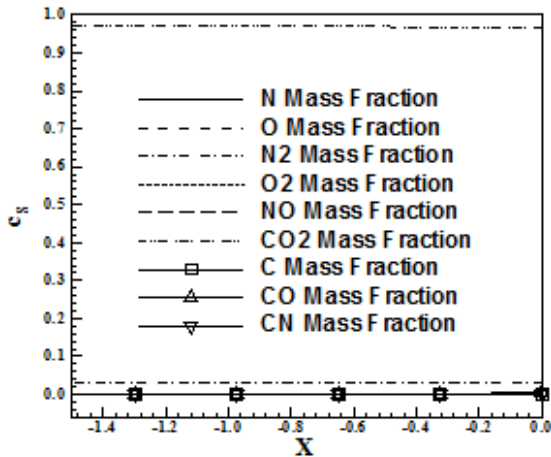


Figure 12. Mass fraction distributions at the stagnation line ([8]).

Viscous, first order, structured results. Figures 13 and 14 exhibit the pressure contours obtained by the [3] and the [8] schemes, respectively, in the viscous case. As can be observed, the pressure field generated by the [3] scheme is more severe than that generated by the [8] scheme. Moreover, the shock region generated by the [8] scheme is slightly closer to the blunt nose than the same region generated by the [3] scheme. This behavior suggests that the shock profile of the [8] scheme is more realistic, closer to the blunt nose. The shock is accurately generated by both schemes and with better characteristics than the inviscid shock.

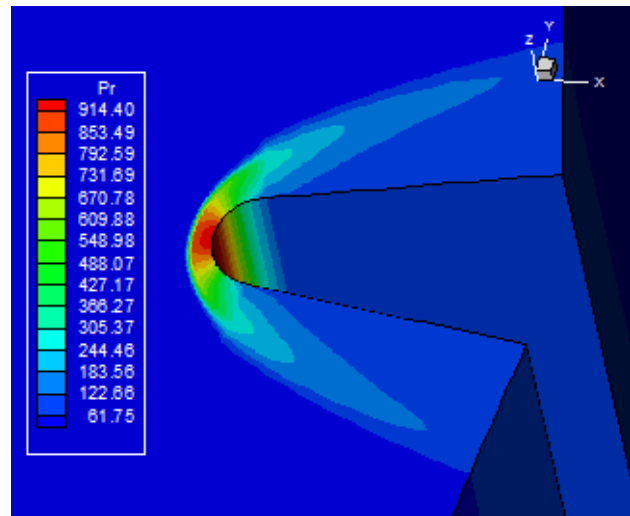


Figure 14. Pressure contours ([8]).

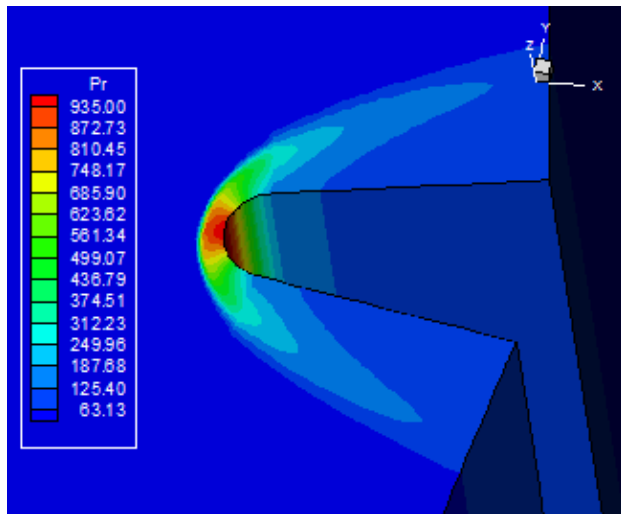


Figure 13. Pressure contours ([3]).

Figures 15 and 16 present the Mach number contours obtained by the [3] and the [8] schemes, respectively. The [3] solution is more dissipative, generating bigger regions of supersonic flow, close to the wall. The [3] solution is more severe.

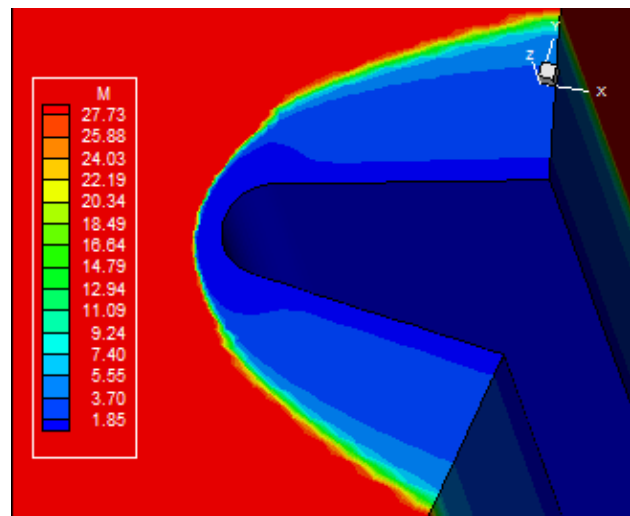


Figure 15. Mach number contours ([3]).

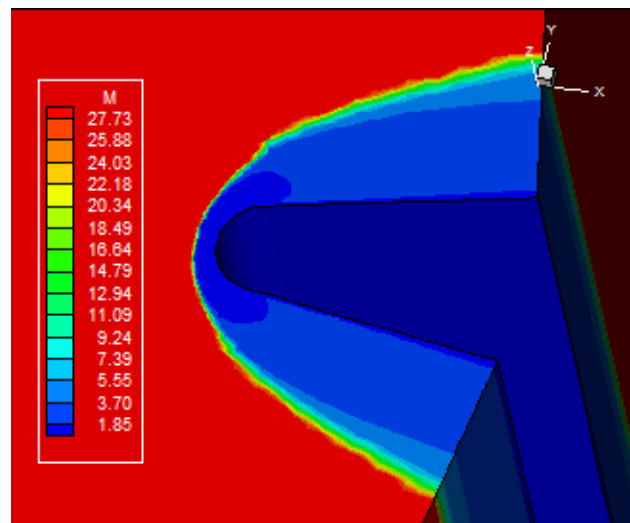


Figure 16. Mach number contours ([8]).

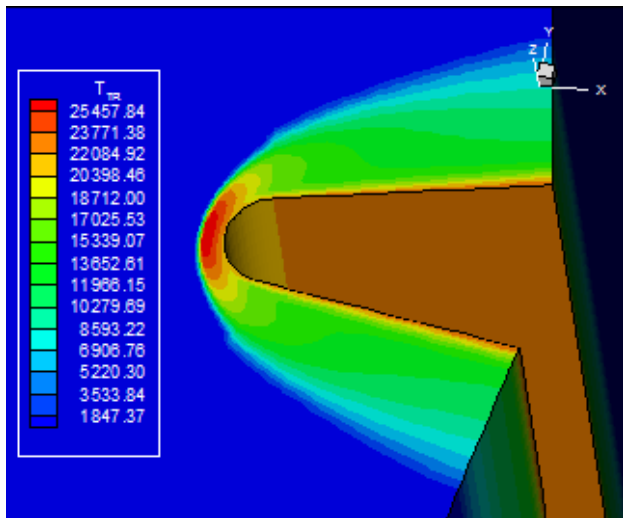


Figure 17. Translational/rotational temperature contours ([3]).

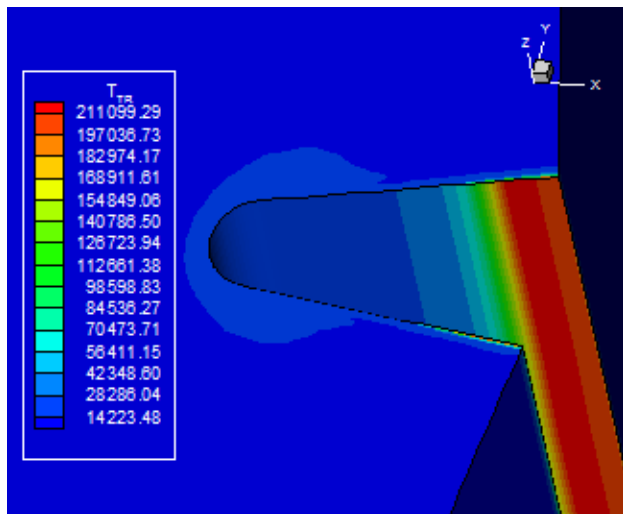


Figure 18. Translational/Rotational temperature contours ([8]).

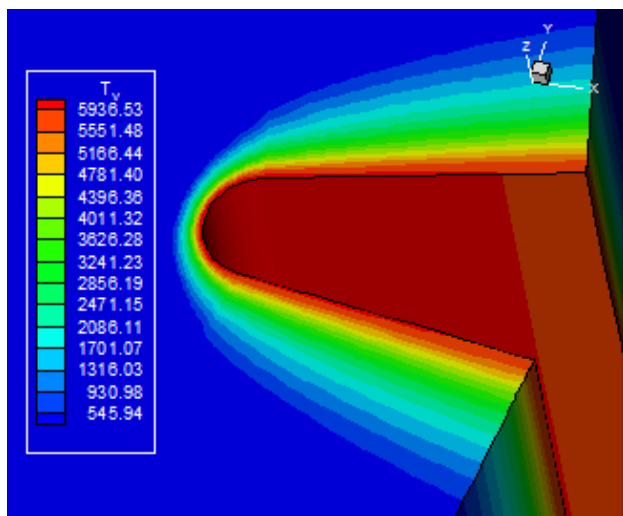


Figure 19. Vibrational temperature contours ([3]).

Figures 17 and 18 exhibit the translational/rotational temperature contours generated by the [3] and the [8] schemes, respectively. In this viscous case, temperatures peaks above

21,000K are observed. In this range, the radiation heat transfer phenomenon is predominant and justifies the use of a blunt slender body to fly at the Mars atmosphere. The normal shock wave generated by the [3] scheme is more symmetrical and heater than the [8] one. The [8] solution presents problems with the shock formation and the contours are severely damaged.

Figures 19 and 20 show the vibrational temperature contours obtained by the [3] and the [8] algorithms, respectively. The vibrational temperature field generated by the [3] scheme is more strength than the respective one due to [3]. Moreover, the [8] shock layer is confined to a smaller region, close to the wall, than the [3] shock layer region.

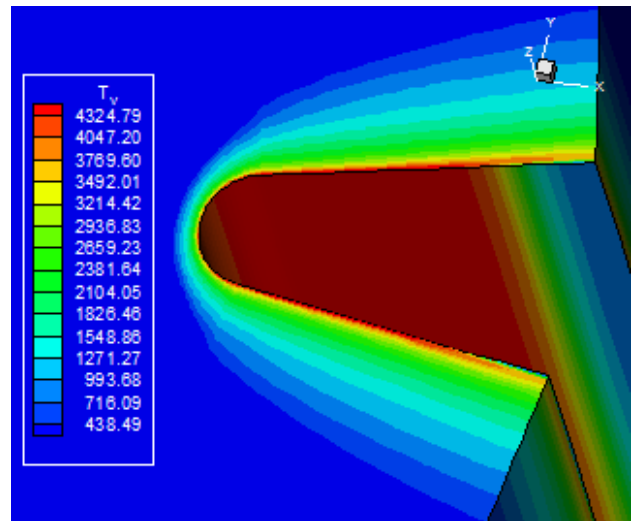


Figure 20. Vibrational temperature contours ([8]).

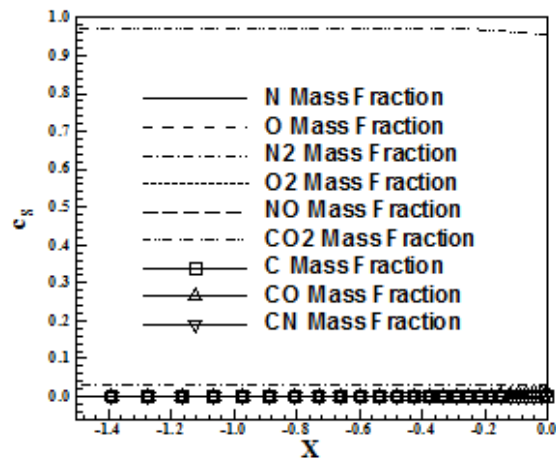


Figure 21. Mass fraction distributions at the stagnation line ([3]).

Figure 21 exhibits the mass fraction distributions of the nine species obtained from the [3] scheme. A discrete dissociation of the CO₂ is observed. As also noted the formation of CO is very discrete.

Figure 22 shows the mass fraction distributions of the nine species obtained from the [8] scheme. A discrete dissociation of CO₂, close to the blunt nose, is seen. It is not perceptible the formation of CO.

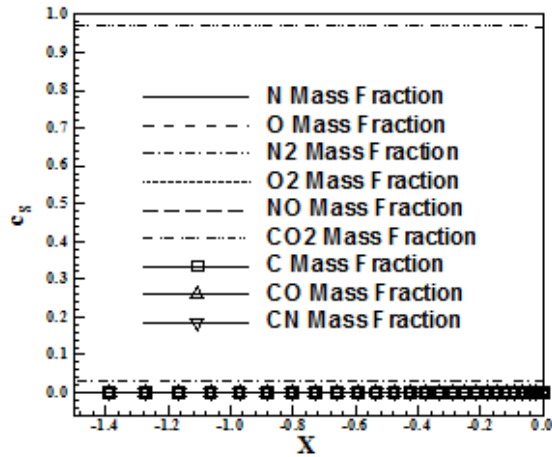


Figure 22. Mass fraction distributions at the stagnation line ([8]).

Inviscid, second order, structured results. Figures 23 and 24 show the pressure contours obtained by the [3] and the [8] schemes, respectively. The most strength pressure field is due to [8]. Both solutions present good symmetry properties. The pressure peak due to [3] reaches a value of 715 unities, whereas this peak due to [8] reaches a value of 738, identifying the latter as more conservative.

Figures 29 and 30 show the vibrational temperature contours obtained by [3] and by [8] schemes, respectively. The hot shock layer of the [8] solution is confined to a smaller region than the hot shock layer of the [3] solution. The [3] solution is smoother than the [8] one. Moreover, the [8] solution is more intense than the respective one of [3].

inviscid results. Again these peaks are concentrated in the blunt nose region.

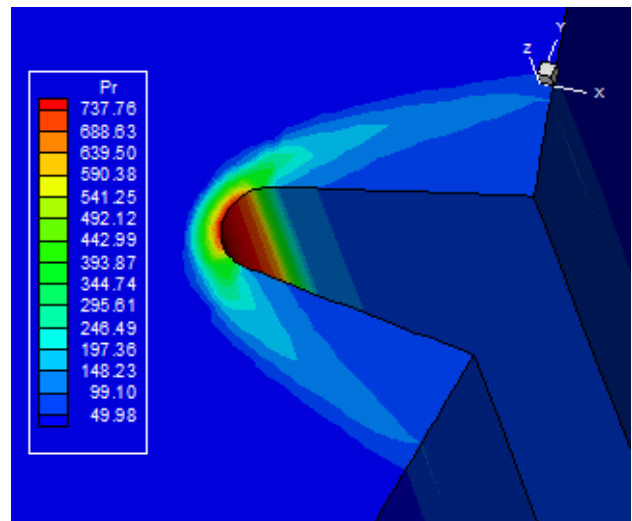


Figure 24. Pressure contours ([8]).

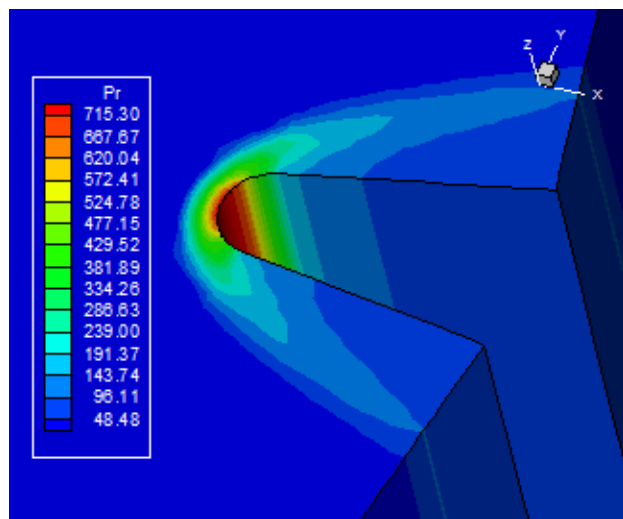


Figure 23. Pressure contours ([3]).

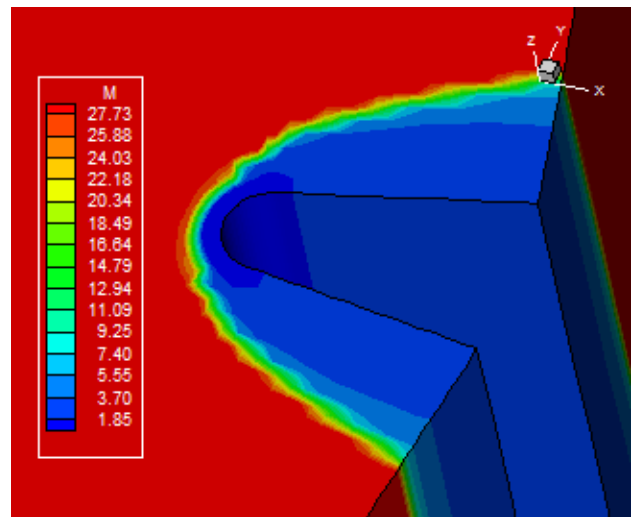


Figure 25. Mach number contours ([3]).

Figures 25 and 26 present the Mach number contours due to [3] and [8], respectively. The two Mach number fields are very similar, quantitatively and qualitatively.

Figures 27 and 28 show the translational/rotational temperature contours obtained by [3] and [8], respectively. The temperature fields due to [3] and [8] reach maximum peaks of 22,644K and 22,610K, less intense than in the

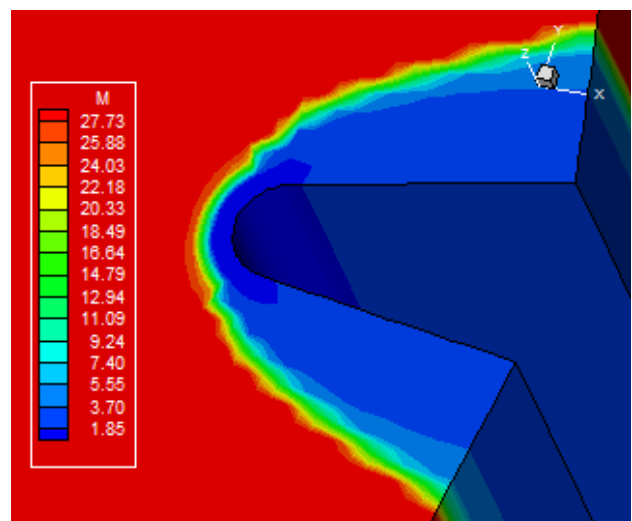


Figure 26. Mach number contours ([8]).

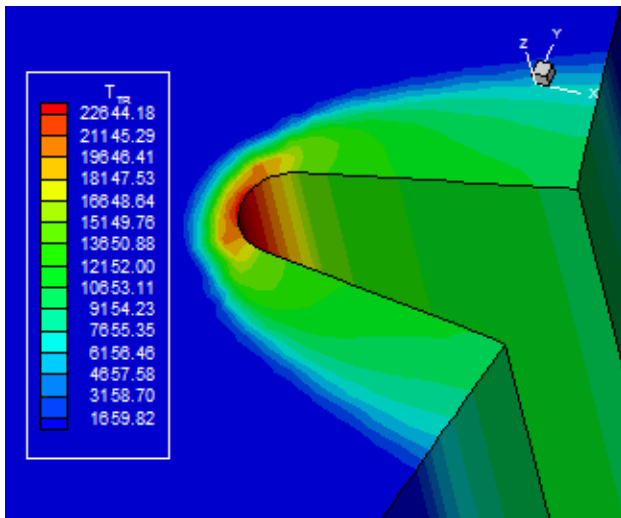


Figure 27. Translational/rotational temperature contours ([3]).

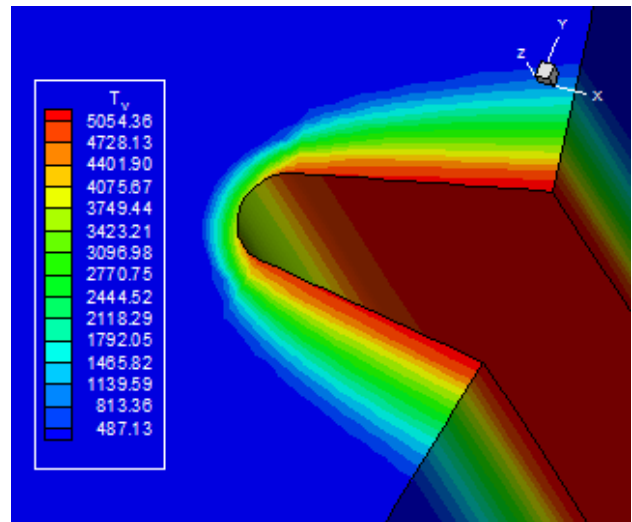


Figure 30. Vibrational temperature contours ([8]).

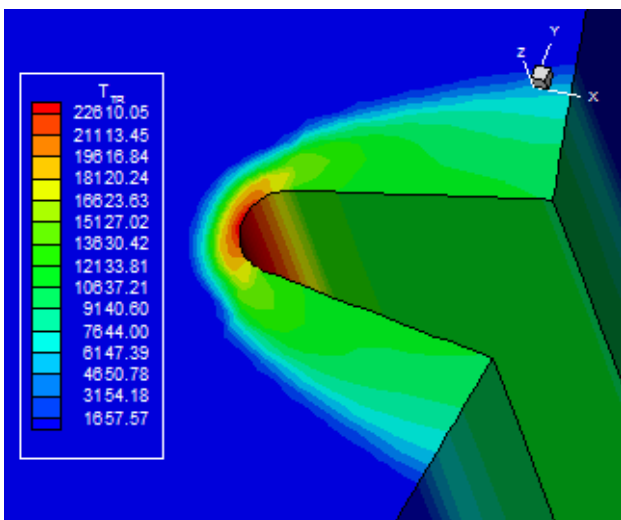


Figure 28. Translational/rotational temperature contours ([8]).

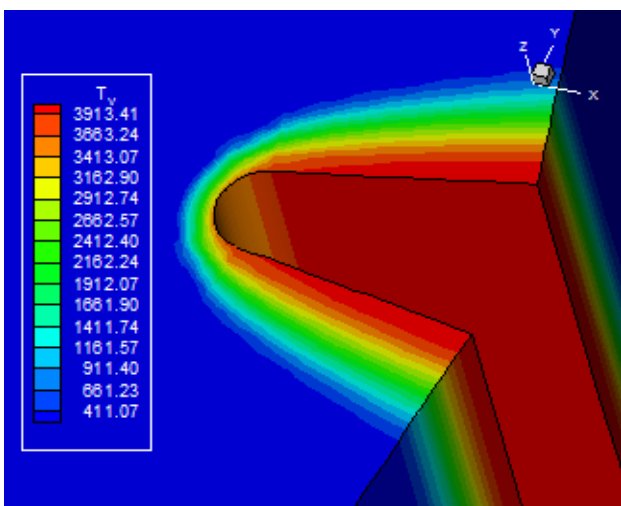


Figure 29. Vibrational temperature contours ([3]).

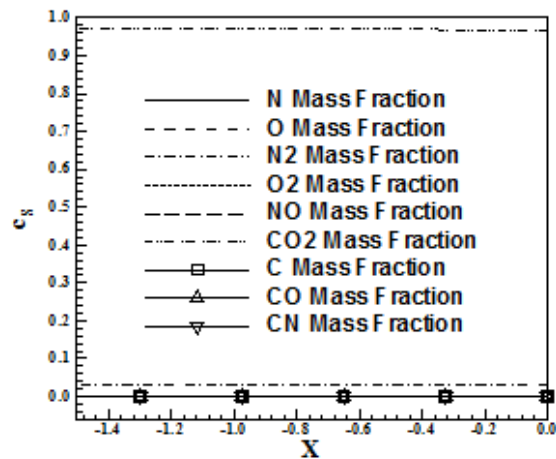


Figure 31. Mass fraction distributions at the stagnation line ([3]).

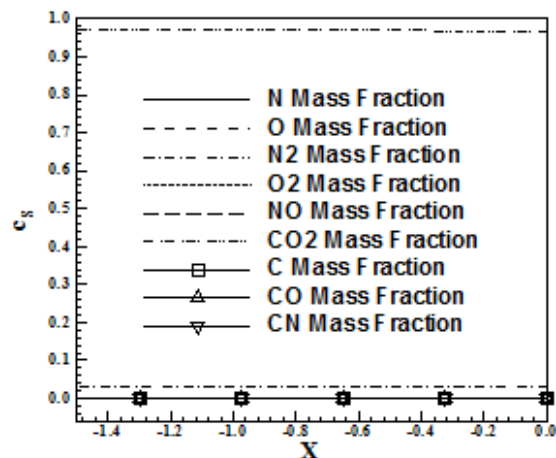


Figure 32. Mass fraction distributions at the stagnation line ([8]).

Figure 31 exhibits the mass fraction distributions along the body stagnation line obtained by the [3] scheme. Again a very discrete dissociation of the CO_2 is observed. The formation of CO and O are also almost non-perceptible.

Figure 32 presents the mass fraction distributions generated by the [8] algorithm. It is possible to note a discrete CO_2 dissociation than in the [3] case. As a consequence, the CO and O formations are also almost non-perceptible. The production of C and CN is less pronounced.

Viscous, second order, structured results. In this case, only the [3] scheme has produced converged results. Figure 33 exhibits the pressure contours obtained by the [3]. The shock wave is well captured. Good symmetry properties are observed in the [3] solution.

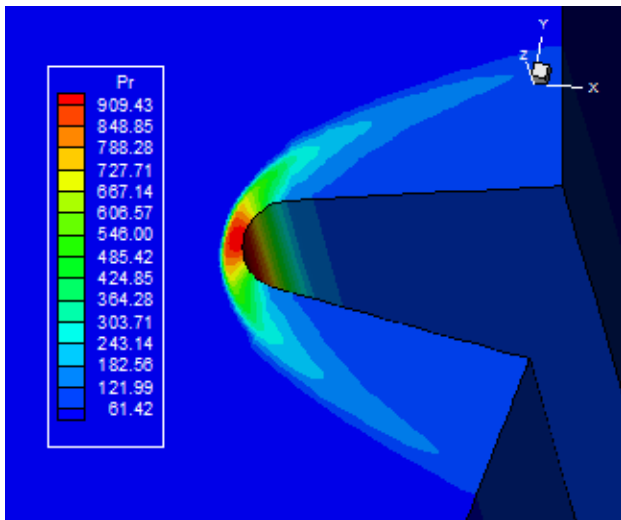


Figure 33. Pressure contours ([3]).

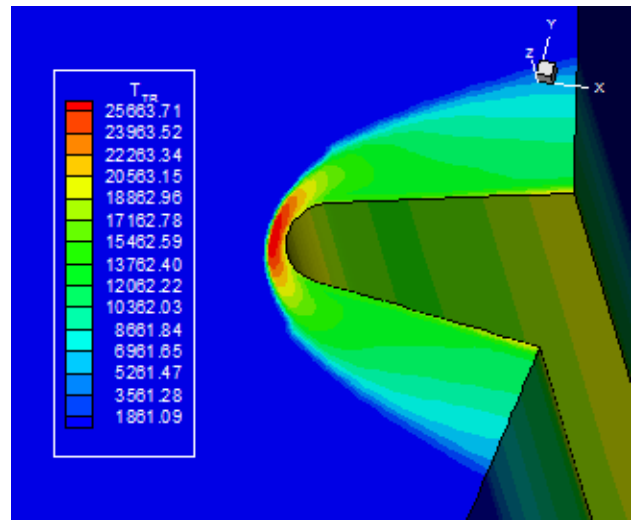


Figure 35. Translational/rotational temperature contours ([3]).

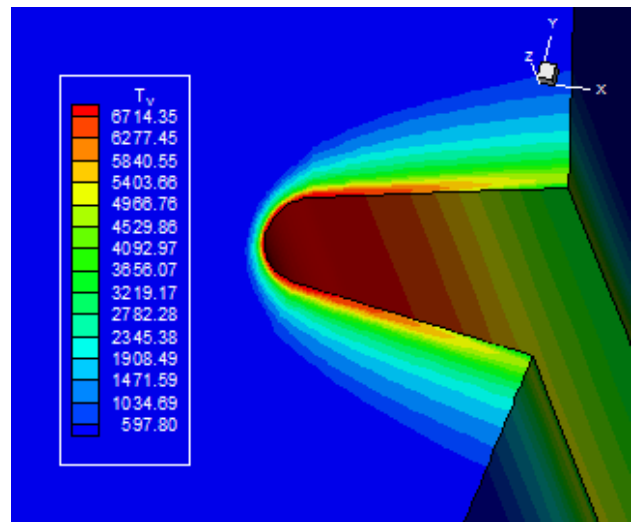


Figure 36. Vibrational temperature contours ([3]).

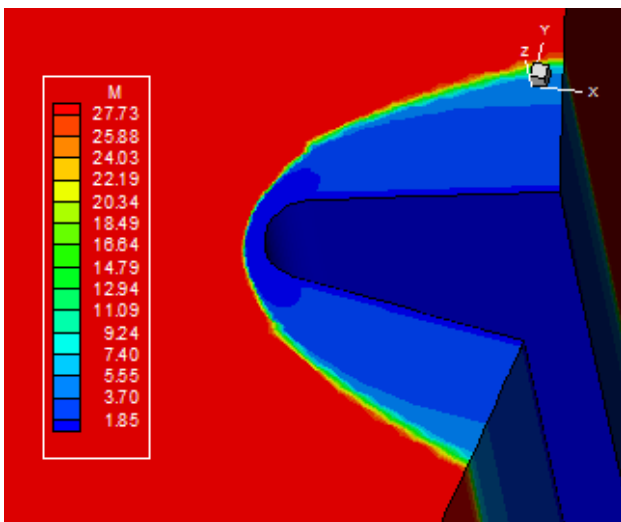


Figure 34. Mach number field ([3]).

Figure 34 shows the Mach number contours generated by [3] algorithm. As can be observed, the [3] scheme is more dissipative, spreading the low supersonic region around the body. The contours of Mach number due to [3] are symmetrical enough. The shock wave develops correctly, passing from a normal shock wave, going to oblique shock waves and finishing with Mach waves.

Figure 35 shows the translational/rotational temperature contours obtained by [3] scheme. The [3] temperature field is close to 26,000K. It is clear the high temperature at the body nose.

Figure 36 presents the vibrational temperature contours obtained from [3] scheme. The [3] solution presents a more severe temperature field in relation to its inviscid counterpart. The shock layer of [3] is confined to a small region.

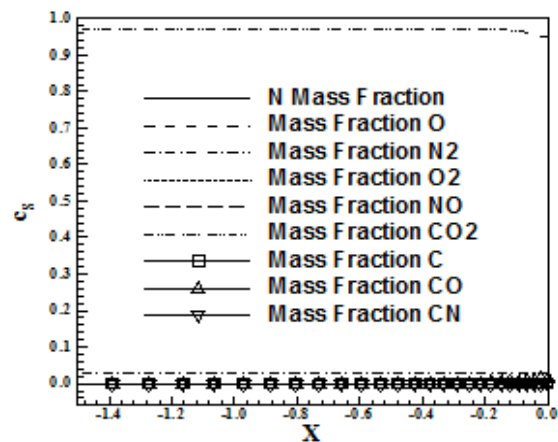


Figure 37. Mass fraction distributions at the stagnation line ([3]).

Figure 37 exhibits the mass fraction distributions along the stagnation line of the blunt body, generated by [3] scheme. As can be seen, a meaningful dissociation of CO₂ is captured by the [3] scheme, with significant formation of CO.

Computational data. The computational data of the present simulations are shown in Tab. 8. The best performance, converging in a minor number of iterations and wasting minor time, is due to the [3] scheme, first-order and inviscid case. The [8] did not present converged results to the second-order viscous case. The convergence to 3 o.r.r. is the minimum acceptable to consider a converged result. This happens in three cases. All solutions are of good quality.

Table 8. Computational data.

Case	CFL	Iterations	o.r.r. ⁽¹⁾
[3] – 1st – Inviscid	0.2	1,387	4
[8] – 1st – Inviscid	0.1	3,951	4
[3] – 1st – Viscous	0.2	3,960	4
[8] – 1st – Viscous	0.1	6,225	3
[3] – 2nd – Inviscid	0.1	3,114	4
[8] – 2nd – Inviscid	0.1	4,105	3
[3] – 2nd – Viscous	0.2	2,414	3

⁽¹⁾: o.r.r. = order of residual reduction.

X. CONCLUSIONS

This work, first part of this study, describes a numerical tool to perform thermochemical non-equilibrium simulations of reactive flow in three-dimensions. The [3] and [8] schemes, in their first- and second-order versions, are implemented to accomplish the numerical simulations. The Euler and Navier-Stokes equations, on a finite volume context and employing structured and unstructured spatial discretizations, are applied to solve the “hot gas” hypersonic flow around a blunt body, in three-dimensions. The second-order version of the [3] and [8] schemes are obtained from a “MUSCL” extrapolation procedure (details in [10]) in a context of structured spatial discretization. In the unstructured context, only first-order solutions are obtained. The convergence process is accelerated to the steady state condition through a spatially variable time step procedure, which has proved effective gains in terms of computational acceleration (see [4-5]).

The reactive simulations involve a Mars atmosphere chemical model of nine species: N, O, N₂, O₂, NO, CO₂, C, CO, and CN. Fifty-three chemical reactions, involving dissociation and recombination, are simulated by the proposed model. The Arrhenius formula is employed to determine the reaction rates and the law of mass action is used to determine the source terms of each gas species equation.

The results have demonstrated that the most conservative scheme is due to [8], although the [3] scheme is more robust, providing results to the second-order viscous case. Moreover, the [3] scheme presents the best mass fraction profiles at the stagnation line, characterizing discrete dissociation of CO₂ and formation of CO.

REFERENCES

- [1] ESA, MARSNET – Assessment Study Report, *ESA Publication SCI* (91) 6, January, 1991.
- [2] E. S. G. Maciel, and A. P. Pimenta, Thermochemical Non-Equilibrium Reentry Flows in Two-Dimensions – Part I, *WSEAS TRANSACTIONS ON MATHEMATICS*, Vol. 11, Issue 6, June, 2012, pp. 520-545.
- [3] B. Van Leer, Flux-Vector Splitting for the Euler Equations, *Lecture Notes in Physics*. Springer Verlag, Berlin, Vol. 170, 1982, pp. 507-512.
- [4] E. S. G. Maciel, Analysis of Convergence Acceleration Techniques Used in Unstructured Algorithms in the Solution of Aeronautical Problems – Part I, *Proceedings of the XVIII International Congress of Mechanical Engineering (XVIII COBEM)*, Ouro Preto, MG, Brazil, 2005. [CD-ROM]
- [5] E. S. G. Maciel, Analysis of Convergence Acceleration Techniques Used in Unstructured Algorithms in the Solution of Aerospace Problems – Part II, *Proceedings of the XII Brazilian Congress of Thermal Engineering and Sciences (XII ENCIT)*, Belo Horizonte, MG, Brazil, 2008. [CD-ROM]
- [6] E. S. G. Maciel, and Pimenta, A. P., Thermochemical Non-Equilibrium Reentry Flows in Three-Dimensions – Part I – Structured Solutions, *WSEAS TRANSACTIONS ON APPLIED AND THEORETICAL MECHANICS*, Vol. 8, Issue 1, January, 2013, pp. 1-25.
- [7] E. S. G. Maciel, and Pimenta, A. P., Thermochemical Non-Equilibrium Reentry Flows in Three-Dimensions: Seven Species Model – Part I – Structured Solutions, *WSEAS TRANSACTIONS ON MATHEMATICS* (under review).
- [8] M. Liou, and C. J. Steffen Jr., A New Flux Splitting Scheme, *Journal of Computational Physics*, Vol. 107, 1993, pp. 23-39.
- [9] F. G. Blottner, Viscous Shock Layer at the Stagnation Point With Nonequilibrium Air Chemistry, *AIAA Journal*, Vol. 7, No. 12, 1969, pp. 2281-2288.
- [10] C. Hirsch, Numerical Computation of Internal and External Flows – Computational Methods for Inviscid and Viscous Flows. John Wiley & Sons Ltd, 691p, 1990.
- [11] R. K. Prabhu, An Implementation of a Chemical and Thermal Nonequilibrium Flow Solver on Unstructured Meshes and Application to Blunt Bodies, *NASA CR-194967*, 1994.
- [12] S. K. Saxena and M. T. Nair, An Improved Roe Scheme for Real Gas Flow, *AIAA Paper 2005-587*, 2005.
- [13] R. D. Kay, and M. P. Netherfield, Thermochemical Non-Equilibrium Computations for a Mars Entry Vehicle, *AIAA Paper 93-2841*, July, 1993.
- [14] J. Evans, W. L. Grose, and C. J. Schexnayder, Effects of Nonequilibrium Ablation Chemistry on Viking Radio Blackout, *AIAA Paper 73-0260*, 1973.
- [15] C. Park, G. V. Candler, J. T. Howe, and R. L. Jaffe, Chemical-Kinetic Problems of Future NASA Missions, *AIAA Paper 91-0464*, 1991.
- [16] Table of Recommended Rate Constants for Chemical Reactions Occurring in Combustion, *NSRDS-NBS 67*, April, 1980.
- [17] G. F. Mitchell, and T. J. Deveau, Effects of a Shock on Diffuse Interstellar Cloud, *J. Astrophysics*, No. 266, 1983, pp. 646-661.
- [18] F. G. Blottner, M. Johnson, and M. Ellis, Chemically Reacting Viscous Flow Program for Multi-Component Gas Mixtures, *SC-RR-70-754*, Sandia Laboratories, December, 1971.
- [19] G. V. Candler, Computation of Thermochemical Non-Equilibrium Martian Atmospheric Entry Flows, *AIAA Paper 90-1695*, 1990.
- [20] R. N. Gupta, K. P. Lee, J. N. Moss, and K. Sutton, Viscous Shock Layer Solutions with Coupled Radiation and Ablation Injection for Earth Entry, *AIAA Paper 90-1697*, 1990.
- [21] C. R. Wilke, A Viscosity Equation for Gas Mixtures, *J. Chem. Phys.*, Vol. 18, No. 4, 1950, p. 517.
- [22] G. V. Candler, and R. W. MacCormack, The Computation of Hypersonic Ionized Flows in Chemical and Thermal Non-Equilibrium, *AIAA Paper 88-0511*, 1988.
- [23] L. Landau, and E. Teller, Theory of Sound Dispersion, *Physikalische Zeitschrift Der Sowjetunion*, Vol. 10, 1936, pp. 34-43.
- [24] R. C. Millikan and D. R. White, Systematics of Vibrational Relaxation, *The Journal of Chemical Physics*, Vol. 39, No. 12, 1963, pp. 3209-3213.
- [25] R. Monti, D. Paterna, R. Savino, and A. Esposito, Experimental and Numerical Investigation on Martian Atmosphere Entry, *AIAA Paper 2001-0751*, 2001.
- [26] A. F. P. Houwing, S. Nonaka, H. Mizuno, and K. Takayama, Effects of Vibrational Relaxation on Bow Shock Stand-off Distance for Nonequilibrium Flows, *AIAA Journal*, Vol. 38, No. 9, 2000, pp. 1760-1763.

- [27] C. Park, Assessment of Two-Temperature Kinetic Model for Ionizing Air, *Journal of Thermophysics and Heat Transfer*, Vol. 3, No. 13, pp. 233-244, 1989.
- [28] D. Ait-Ali-Yahia, and W. G. Habashi, Finite Element Adaptive Method for Hypersonic Thermochemical Nonequilibrium Flows, *AIAA Journal* Vol. 35, No. 8, 1997, 1294-1302.
- [29] E. S. G. Maciel, TVD Algorithms Applied to the Solution of the Euler and Navier-Stokes Equations in Three-Dimensions, *WSEAS TRANSACTIONS ON MATHEMATICS*, Vol. 11, Issue 6, June, 2012, pp. 546-572.
- [30] R. Radespiel, and N. Kroll, Accurate Flux Vector Splitting for Shocks and Shear Layers, *Journal of Computational Physics*, Vol. 121, 1995, pp. 66-78.
- [31] L. N. Long, M. M. S. Khan, and H. T. Sharp, Massively Parallel Three-Dimensional Euler / Navier-Stokes Method, *AIAA Journal*, Vol. 29, No. 5, 1991, pp. 657-666.
- [32] B. Van Leer, Towards the Ultimate Conservative Difference Scheme. II. Monotonicity and Conservation Combined in a Second-Order Scheme, *Journal of Computational Physics*, Vol. 14, 1974, pp. 361-370.
- [33] P. L. Roe, In *Proceedings of the AMS-SIAM Summer Seminar on Large-Scale Computation in Fluid Mechanics*, Edited by B. E. Engquist et al, *Lectures in Applied Mathematics*, Vol. 22, 1983, p. 163.
- [34] E. S. G. Maciel, Simulação Numérica de Escoamentos Supersônicos e Hipersônicos Utilizando Técnicas de Dinâmica dos Fluidos Computacional, *Doctoral Thesis*, ITA, CTA, São José dos Campos, SP, Brazil, 258p, 2002.
- [35] NASA, Models of Mars' Atmosphere [1974], *NASA SP-8010*.



Edisson S. G. Maciel (F'14), born in 1969, february, 25, in Recife, Pernambuco. He is a Mechanical Engineering undergraduated by UFPE in 1992, in Recife, PE, Brazil; Mester degree in Thermal Engineering by UFPE in 1995, in Recife, PE, Brazil; Doctor degree in Aeronautical Engineering by ITA in 2002, in São José dos Campos, SP, Brazil; and Post-Doctor degree in Aeronautical

Engineering by ITA in 2009, in São José dos Campos, SP, Brazil

Actually, he is doing a new post-doctorate curse in Aerospace Engineering at ITA. The last researches are based on thermochemical non-equilibrium reentry simulations in Earth and thermochemical non-equilibrium entry simulations in Mars. They are: Maciel, E. S. G., and Pimenta, A. P., "Thermochemical Non-Equilibrium Reentry Flows in Two-Dimensions – Part I", *WSEAS Transactions on Mathematics*, Vol. 11, Issue 6, June, pp. 520-545, 2012; Maciel, E. S. G., and Pimenta, A. P., "Thermochemical Non-Equilibrium Entry Flows in Mars in Two-Dimensions – Part I", *WSEAS Transactions on Applied and Theoretical Mechanics*, Vol. 8, Issue 1, January, pp. 26-54, 2013; and he has three published books, the first one being: Maciel, E. S. G., "Aplicações de Algoritmos Predictor-Corretor e TVD na Solução das Equações de Euler e de Navier-Stokes em Duas Dimensões", Recife, PE, Editor UFPE, 2013. He is interested in the Magnetogasdynamic field with applications to fluid dynamics and in the use of ENO algorithms.